

CM² MAGAZINE



第 96 期



南方科技大学海洋磁学中心主编

<http://cm2.sustech.edu.cn/>

创刊词

海洋是生命的摇篮，是文明的纽带。地球上最早的生命诞生于海洋，海洋里的生命最终进化成了人类，人类的文化融合又通过海洋得以实现。人因海而兴。

人类对海洋的探索从未停止。从远古时代美丽的神话传说，到麦哲伦的全球航行，再到现代对大洋的科学钻探计划，海洋逐渐从人类敬畏崇拜幻想的精神寄托演变成可以开发利用与科学研究的客观存在。其中，上个世纪与太空探索同步发展的大洋科学钻探计划将人类对海洋的认知推向了崭新的纬度：深海（deep sea）与深时（deep time）。大洋钻探计划让人类知道，奔流不息的大海之下，埋藏的却是亿万年的地球历史。它们记录了地球板块的运动，从而使板块构造学说得到证实；它们记录了地球环境的演变，从而让古海洋学方兴未艾。

在探索海洋的悠久历史中，从大航海时代的导航，到大洋钻探计划中不可或缺的磁性地层学，磁学发挥了不可替代的作用。这不是偶然，因为从微观到宏观，磁性是最基本的物理属性之一，可以说，万物皆有磁性。基于课题组的学科背景和对海洋的理解，我们对海洋的探索以磁学为主要手段，海洋磁学中心因此而生。

海洋磁学中心，简称 CM^2 ，一为其全名“Centre for Marine Magnetism”的缩写，另者恰与爱因斯坦著名的质能方程 $E = MC^2$ 对称，借以表达我们对科学巨匠的敬仰和对科学的不懈追求。

然而科学从来不是单打独斗的产物。我们以磁学为研究海洋的主攻利器，但绝不仅限于磁学。凡与磁学相关的领域均是我们关注的重点。为了跟踪反映国内外地球科学特别是与磁学有关的地球科学领域的最新研究进展，海洋磁学中心特地主办 CM^2 Magazine，以期与各位地球科学工作者相互交流学习、合作共进！

“海洋孕育了生命，联通了世界，促进了发展”。21世纪是海洋科学的时代，由陆向海，让我们携手迈进中国海洋科学的黄金时代。

目录

1. 晚第四纪热带与亚热带地区快速气候变化：热带水汽变化事件的大陆信号	1
2. 幔源岩浆中的轻氧同位素反映了大陆岩石圈地幔物质的同化作用	3
3. 来自 Manita peć 洞穴(克罗地亚的 Velebit 山)的石笋揭示的末次冰期期间水文气候的变化.....	6
4. 4200-2800 年前中国西北地区异常温暖.....	10
5. 调和超大陆旋回模型与古俯冲带	14
6. 地幔柱和其在地球过程中的作用	16
7. 古新世/始新世期间火山活动驱动的碳反馈	19
8. 纳米流动与地震不稳定性.....	23
9. 喜马拉雅 Sikkim 褶皱逆断层带磁组构与应变组构的运动学方法.....	26
10. 中古生代以来以大陆岛弧为主的全球化学风化作用	29
11. 二叠纪、三叠纪地磁场长期变化及对古地磁场特征的指示	31
12. IODP U1504 孔多期碳酸盐岩脉记录了南海边缘早白垩世至早新生代伸展事件 ...	35

1. 晚第四纪热带与亚热带地区快速气候变化：热带水汽变化事件的大陆信号

翻译人：仲义 zhongy@sustech.edu.cn



Bradley R S, Diaz H F, Late Quaternary Abrupt Climate Change in the Tropics and Sub-Tropics: The Continental Signal of Tropical Hydroclimate Events (THEs) [J]. Reviews of Geophysics, 59(4), 2021, e2020RG000732.

<https://doi.org/10.1029/2020RG000732>

摘要：热带水汽事件表现为极端的区域性降水异常变化，在海洋氧同位素 2-4 期重复性出现，并涉及到晚第四纪最突然和剧烈的气候变化。这些异常普遍存在于整个热带地区，是哈德雷环流和热带辐合带（ITCZ）共同的结果，受控于区域性因子调节的对流降水。湖泊沉积物、石笋、和近海沉积物整合了整个内陆大陆环境变化，为过去约 7 万年间大陆变化提供综合性记录。虽然其他地区记录大多降水增多，但是大多数区域经历了严重的干旱化。由于年代学不确定性，这些热带降水异常发生的时间（ $\pm 100-1000$ 年）非常接近于北大西洋冰筏碎屑（IRD）沉积指示的海因里希事件（Heinrich events）。IRD 记录是非常好的指示淡水输入的信号，也是导致大西洋经向翻转流（AMOC）强度在每次 Heinrich 事件期间剧烈减弱所必须的。由于 AMOC 的减少和海冰面积的突然扩张，北大西洋和邻近大陆发生冷却，大气迅速响应，包括 ITCZ 和相关降雨带的南移。这种哈德雷环流大规模改变的气候变化的结果受到区域性因素的控制，在整个热带地区作为一系列极端水文事件被记录下来。本文综述了这些变化中可能发挥作用的物理机制。

Abstract: Tropical hydroclimatic events, characterized by extreme regional rainfall anomalies, were a recurrent feature of marine isotope stages 2–4 and involved some of the most abrupt and dramatic climatic changes in the late Quaternary. These anomalies were pervasive throughout the tropics and resulted from the southward displacement of the Hadley circulation and the Intertropical Convergence Zone (ITCZ) and its associated convective rainfall, modulated by regional factors. Lake sediments, stalagmites, and offshore marine sediments that integrate inland

continental conditions provide a comprehensive record of these changes over the past ~70,000 yr. Vast areas experienced severe drought while other areas recorded greatly increased rainfall. Within the uncertainties of dating, these tropical rainfall anomalies occurred very close in time ($\pm 10^2$ – 10^3 yr) to the deposition of North Atlantic ice-rafted debris (IRD) that defines Heinrich events (HEs). The IRD record is a good proxy for the amount and distribution of additional freshwater forcing which was necessary to bring about a drastic reduction in the Atlantic Meridional Overturning Circulation (AMOC) strength during each HE. As a consequence of this reduction in AMOC and an abrupt expansion in the area of sea-ice, cooling of the North Atlantic and adjacent continents took place, with a rapid atmospheric response involving the southward displacement of the ITCZ and associated rainfall belts. The climatic consequences of this large-scale change in the Hadley circulation, modulated by regional factors, is clearly recorded throughout the tropics as a series of abrupt and extreme hydroclimatic events. Some of the physical mechanisms that may have played a role in those changes are discussed.

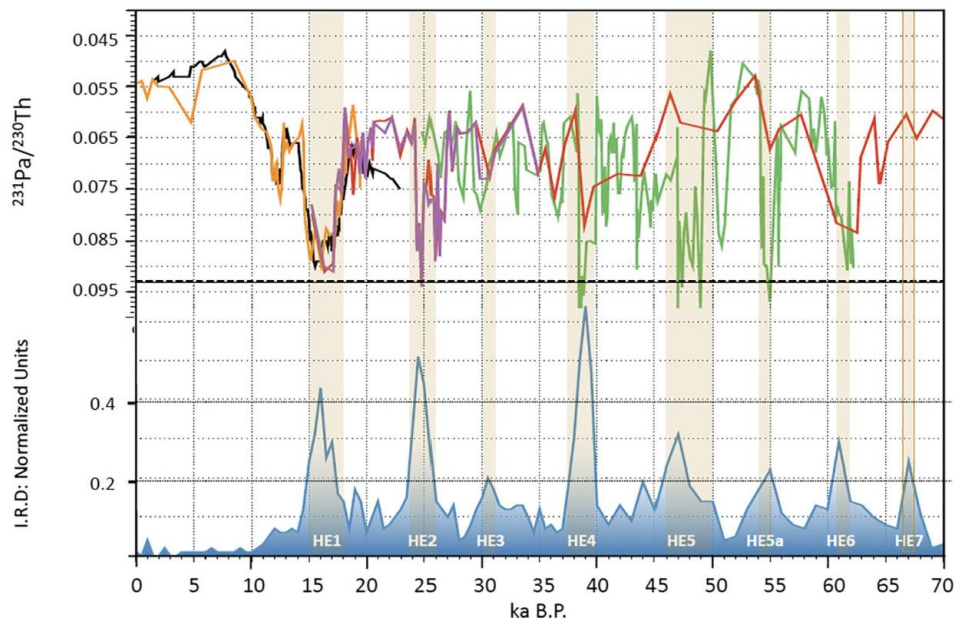


Figure 1. $^{231}\text{Pa}/^{230}\text{Th}$ in several North Atlantic sediment cores; values of >0.093 (dashed black line) represent a complete cessation of North Atlantic deepwater formation (note data are plotted inversely; from McManus et al., 2004, in orange; Lippold et al., 2009, in purple; Böhm, 2014, in red; Henry et al., 2016, in green; Ng et al., 2018, in black, 9-point running mean). Lower blue line is the stacked record of IRD based on 15 North Atlantic cores (normalized values, from Lisiecki & Stern, 2016). Shaded brown intervals indicate times when IRD exceeded median values for MIS2–4.

2. 幔源岩浆中的轻氧同位素反映了大陆岩石圈地幔物质的同化作用



翻译人：冯婉仪 fengwy@sustech.edu.cn

Xu J Y, Giuliani A, Li Q L, et al. Light oxygen isotopes in mantle-derived magmas reflect assimilation of sub-continental lithospheric mantle material [J]. Nature communications, 2021, 12, 6295.

<https://doi.org/10.1038/s41467-021-26668-z>

摘要：幔源岩浆氧同位素比值不同于典型地幔值的主要原因是地壳污染、地幔源区中含有深俯冲循环的地壳物质或原始地幔不均一性。在这里，我们利用金伯利岩（即在上升过程中混染地幔碎片的富碳酸盐岩岩浆）为幔源岩浆中轻氧同位素特征的起源提供了另一种观点。金伯利岩中的橄榄石颗粒通常具有地幔来源的核部和岩浆成因的边部，因此，可以限定地幔围岩和熔体相的成分。世界范围内金伯利岩橄榄石的二次离子质谱（SIMS）分析结果显示，其核部和边部的平均氧同位素组成存在显著的相关性，即从类似地幔 $^{18}\text{O}/^{16}\text{O}$ 值变化至较低的“地壳”值。这一观测结果表明，含低 $^{18}\text{O}/^{16}\text{O}$ 橄榄石捕虏晶的金伯利岩被低 $^{18}\text{O}/^{16}\text{O}$ 的大陆岩石圈地幔物质同化而改变。因此，与大陆岩石圈地幔中地球化学富集域的相互作用可能是导致幔源岩浆具有显著“地壳”特征的重要原因。

ABSTRACT: Oxygen isotope ratios in mantle-derived magmas that differ from typical mantle values are generally attributed to crustal contamination, deeply subducted crustal material in the mantle source or primordial heterogeneities. Here we provide an alternative view for the origin of light oxygen-isotope signatures in mantle-derived magmas using kimberlites, carbonate-rich magmas that assimilate mantle debris during ascent. Olivine grains in kimberlites are commonly zoned between a mantle-derived core and a magmatic rim, thus constraining the compositions of both mantle wall-rocks and melt phase. Secondary ion mass spectrometry (SIMS) analyses of olivine in worldwide kimberlites show a remarkable correlation between mean oxygen-isotope compositions of cores and rims from mantle-like $^{18}\text{O}/^{16}\text{O}$ to lower ‘crustal’ values. This observation indicates that kimberlites entraining low- $^{18}\text{O}/^{16}\text{O}$ olivine xenocrysts are modified by

assimilation of low- $^{18}\text{O}/^{16}\text{O}$ sub-continental lithospheric mantle material. Interaction with geochemically-enriched domains of the sub-continental lithospheric mantle can therefore be an important source of apparently ‘crustal’ signatures in mantle-derived magmas.

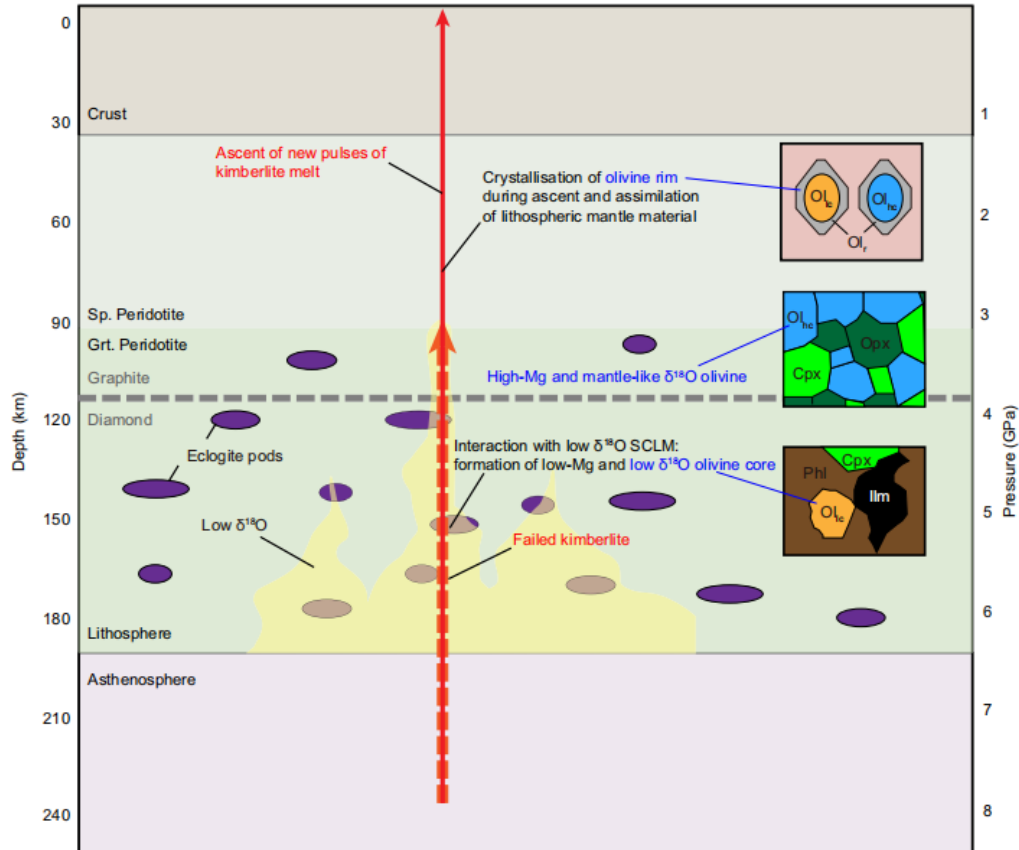


Figure 1. Schematic illustration showing the genesis of oxygen isotope variations in the cores and rims of kimberlitic olivine. High-Mg olivine cores with mantle-like $\delta^{18}\text{O}$ represent xenocrysts derived from coarse-grained granular peridotites. Failed pulses of kimberlite magma may interact with low- $\delta^{18}\text{O}$ metasomatic lithologies (\pm eclogites) in the sub-continental lithospheric mantle (SCLM) and generate low-Mg, low- $\delta^{18}\text{O}$ olivine including olivine megacrysts and olivine in polymict breccias. Later pulses of kimberlite magma entrain wall-rock xenoliths and xenocrysts, including olivine, and crystallize olivine rims over cores of variable composition (both high-Mg and low-Mg). If the lithospheric mantle column traversed by kimberlite magmas is sufficiently enriched in metasomatised low- $\delta^{18}\text{O}$ material, which is partially assimilated, the kimberlite melts crystallize low-Mg, low- $\delta^{18}\text{O}$ olivine rims. Ol_{lc} low-Mg olivine core, Ol_{hc} high-Mg olivine core, Cpx clinopyroxene, Opx orthopyroxene, Phl phlogopite, Ilm ilmenite.

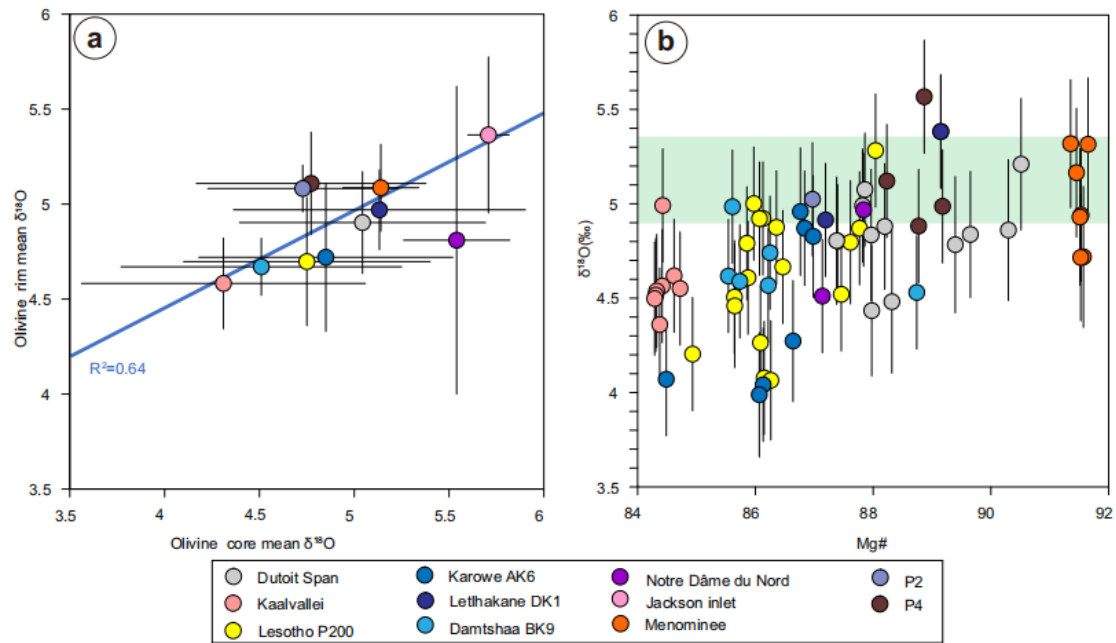


Figure 2. Relationships between the oxygen-isotope composition of olivine rims and cores, and the major-element composition of olivine rims. a Average olivine rim $\delta^{18}\text{O}$ versus average olivine core $\delta^{18}\text{O}$ in the kimberlites (and lamproites) from this study. Error bars are one SD of the mean. The blue line is the linear regression through the data points (excluding the Notre Dâme du Nord outlier). b Covariation diagram showing a broad direct correlation between $\delta^{18}\text{O}$ and Mg# in olivine rims from the examined samples. Error bars indicate the 2σ of each analysis.

3. 来自 Manita peć 洞穴(克罗地亚的 Velebit 山)的石笋揭示的末次冰期期间水文气候的变化



翻译人: 杨会会 11849590@mail.sustech.edu.cn

Suric M, Bajo P, Loncaric R, et al., *Speleothem Records of the Hydroclimate Variability throughout the Last Glacial Cycle from Manita peć Cave (Velebit Mountain, Croatia)* [J]. *Geoscience*, 2021, 11, 347.

<https://doi.org/10.3390/geosciences11080347>

摘要: 本文展示了从克罗地亚 Manita peć 洞穴的两根部分同期生长的石笋标本中获得了稳定碳($\delta^{13}\text{C}$)和氧($\delta^{18}\text{O}$)同位素记录。这个洞穴靠近亚得里亚海海岸(3.7 公里), 海拔 570 米。在整个末次冰期旋回中, 该地经历了地中海和大陆气候竞相影响该区, 并在冰期处于接近冰界的位置。U-Th 定年将石笋的生长阶段限制在深海氧同位素(MIS)5 期至 MIS 3 期和 MIS 2 期至 MIS 1 期的转换期。 ^{14}C 测定法被用来估算一根石笋最年轻部分的年龄, 因为该段石笋含有丰富的碎屑钍, 因此 U-Th 无法测定其年龄。在千年尺度上, $\delta^{18}\text{O}$ 的变化部分响应了格陵兰冰芯(GI)从 GI 22 到 GI 13 的 Dansgaard-Oeschger 旋回。我们将 $\delta^{18}\text{O}$ 记录解释为降水量/水汽来源的变化, 而 $\delta^{13}\text{C}$ 记录则解释为土壤生物生产力的变化。后者表明植被覆盖率从 MIS 3 向 MIS 4 发展时总体减少, 偏移约 8‰, 与基岩接近。然而, 即使在最冷的阶段, 当冰缘环境和增强的干旱使地下水长期驻留时, 碳酸溶解仍然是岩溶作用的驱动力。洞穴堆积物的形态随环境条件的变化而变化, 并与淹没洞穴的区域性结果相补充。具体来说, 在冰期/海平面低水位时期, 轻而多孔的方解石沉积成狭窄的剖面, 而在较温暖和潮湿的条件下, 由于海平面高水位, 洞穴的方解石致密, 被淹没的石笋出现裂缝。据推测, 该滨海站点向陆地站点的转变伴随着更多的地形降雨, 从而掩盖了区域环境的变化。

ABSTRACT: We present stable carbon ($\delta^{13}\text{C}$) and oxygen ($\delta^{18}\text{O}$) isotope records from two partially coeval speleothems from Manita peć Cave, Croatia. The cave is located close to the Adriatic coast (3.7 km) at an elevation of 570 m a.s.l. The site experienced competing Mediterranean and continental climate influences throughout the last glacial cycle and was

situated close to the ice limit during the glacial phases. U-Th dating constrains the growth history from Marine Isotope Stage (MIS) 5 to MIS 3 and the transition from MIS 2 to MIS 1. ^{14}C dating was used to estimate the age of the youngest part of one stalagmite found to be rich in detrital thorium and thus undatable by U-Th. On a millennial scale, $\delta^{18}\text{O}$ variations partly mimic the Dansgaard–Oeschger interstadials recorded in Greenland ice cores (Greenland Interstadials, GI) from GI 22 to GI 13. We interpret our $\delta^{18}\text{O}$ record as a proxy for variations in precipitation amount and/or moisture sources, and the $\delta^{13}\text{C}$ record is interpreted as a proxy for changes in soil bioproductivity. The latter indicates a generally reduced vegetation cover towards MIS 3–MIS 4, with shifts of $\sim 8\text{‰}$ and approaching values close to those of the host rock. However, even during the coldest phases, when a periglacial setting and enhanced aridity sustained long-residence-time groundwater, carbonic-acid dissolution remains the driving force of the karstification processes. Speleothem morphology follows changes in environmental conditions and complements regional results of submerged speleothems findings. Specifically, narrow sections of light porous speleothem calcite precipitated during the glacial/stadial sea-level lowstands, while the warmer and wetter conditions were marked with compact calcite and hiatuses in submerged speleothems due to sea-level highstands. Presumably, the transformation of this littoral site to a continental one with somewhat higher amounts of orographic precipitation was a site-specific effect that masked regional environmental changes.

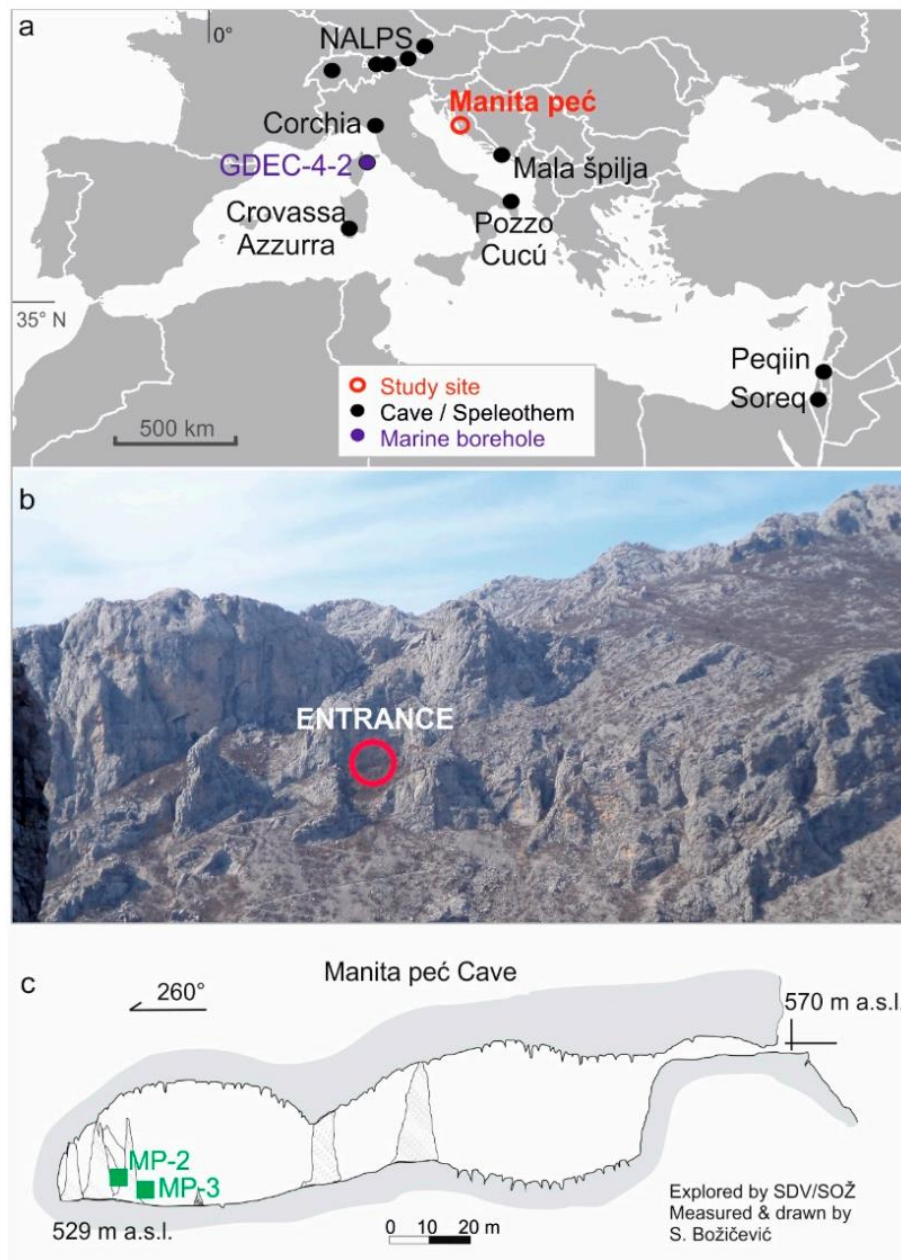


Figure 1. (a) Location of Manita peć Cave and other palaeoclimate archives used for comparison: North Alps (NALPS) caves [4,36], Mala špilja Cave [27], Corchia Cave [15], Crovassa Azzurra Cave [24], Pozzo Cucú Cave [25], Soreq and Peqiin caves [33] and marine borehole GDEC-4-2 [59]. The position of NGRIP ice core, which is not shown here, is 75°5' N, 42°19' W [2]. (b) Cave entrance on the steep and bare side of the Paklenica canyon, Velebit Mountain. (c) Cave survey with marked speleothems positions (green squares and IDs).

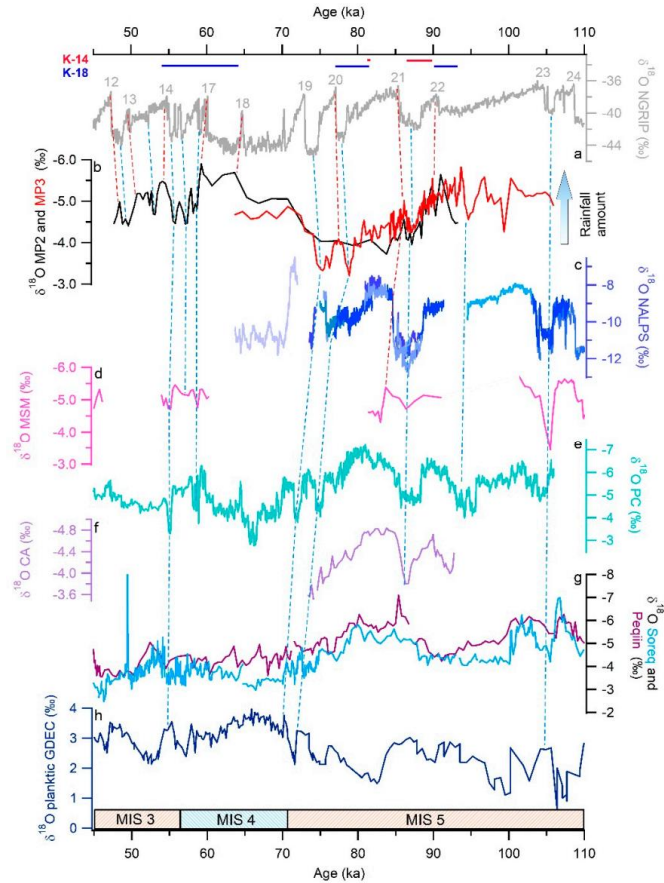


Figure 2. Comparison of $\delta^{18}\text{O}$ records from (a) the NGRIP ice core $\delta^{18}\text{O}$ record [2]; (b) Manita peć Cave stalagmites MP-2 and MP-3; (c) NALPS record from the North Alps caves [4]; (d) Mala Špilja Cave from Mjet Island [27]; (e) Pozzo Cucú Cave [25]; (f) Crovassa Azzurra Cave [24]; (g) Soreq and Peqiin caves in Israel [33]; and (h) marine borehole GDEC-4-2 [59]. Numbers refer to Greenland interstadials. Dashed lines indicate the most prominent matches of recorded stadials (blue) and interstadials (red). Horizontal bars represent growth episodes of speleothems K-14 (red) and K-18 (blue) recovered from the submerged U Vode Pit (Krk Island) [101].

4. 4200-2800 年前中国西北地区异常温暖



翻译人: 李海 12031330@mail.sustech.edu.cn

Jiang Q, Meng B, Wang Z, et al. *Exceptional terrestrial warmth around 4200-2800 years ago in northwest China* [J]. *Science Bulletin*, 2021.

<https://doi.org/10.1016/j.scib.2021.11.001>

摘要: 4200 年前发生的一次持续约 200 年的全新世气候事件造成了文化的中断, 但寒冷/干燥事件后的陆地气候仍不明确, 通常认为青铜器时代 (~4200-2800 yr) 普遍处于寒冷状态。本研究中, 作者报道了一个基于烯酮的过去 12000 年的夏季温度记录, 以及中国西北部的两个烯酮记录, 为事件发生后的气候状况提供了新的见解。研究结果表明, 在全新世长期冷却的趋势下, 4200-2800 年前的青铜器时代出现高达 6 °C 的陆地温度异常。中国西北地区异常温暖, 加上其他地区的异常气候, 表明在 4200-2800 年前太阳活动仍然很高时发生了异常大规模的气候重组, 这对青铜器时代文化发展的气候背景具有重要意义。

ABSTRACT: One of the Holocene abrupt events around 4200 years ago, lasting for ~200 years, is thought to have caused cultural disruptions, yet terrestrial climatic status right after the cold/dry event remains poorly defined and is often presumed that a generally cool condition prevailed during the Bronze Age (~4000–2200 years ago). Here we report an alkenone-based summer temperature record over the past ~12,000 years, in addition to two updated alkenone records, from Northwest China, providing new insights into the climatic status right after the event. Our results indicate that exceptional terrestrial warmth, up to ~6 °C, occurred around 4200–2800 years ago during the Bronze Age, superimposed on the long-term Holocene cooling trend. The exceptional warmth in Northwest China, together with other climate anomalies elsewhere, suggests an unusual large-scale climatic reorganization at 4200–2800 years ago when solar activity remained high, with important implications to the climate background for cultural developments during the Bronze Age.

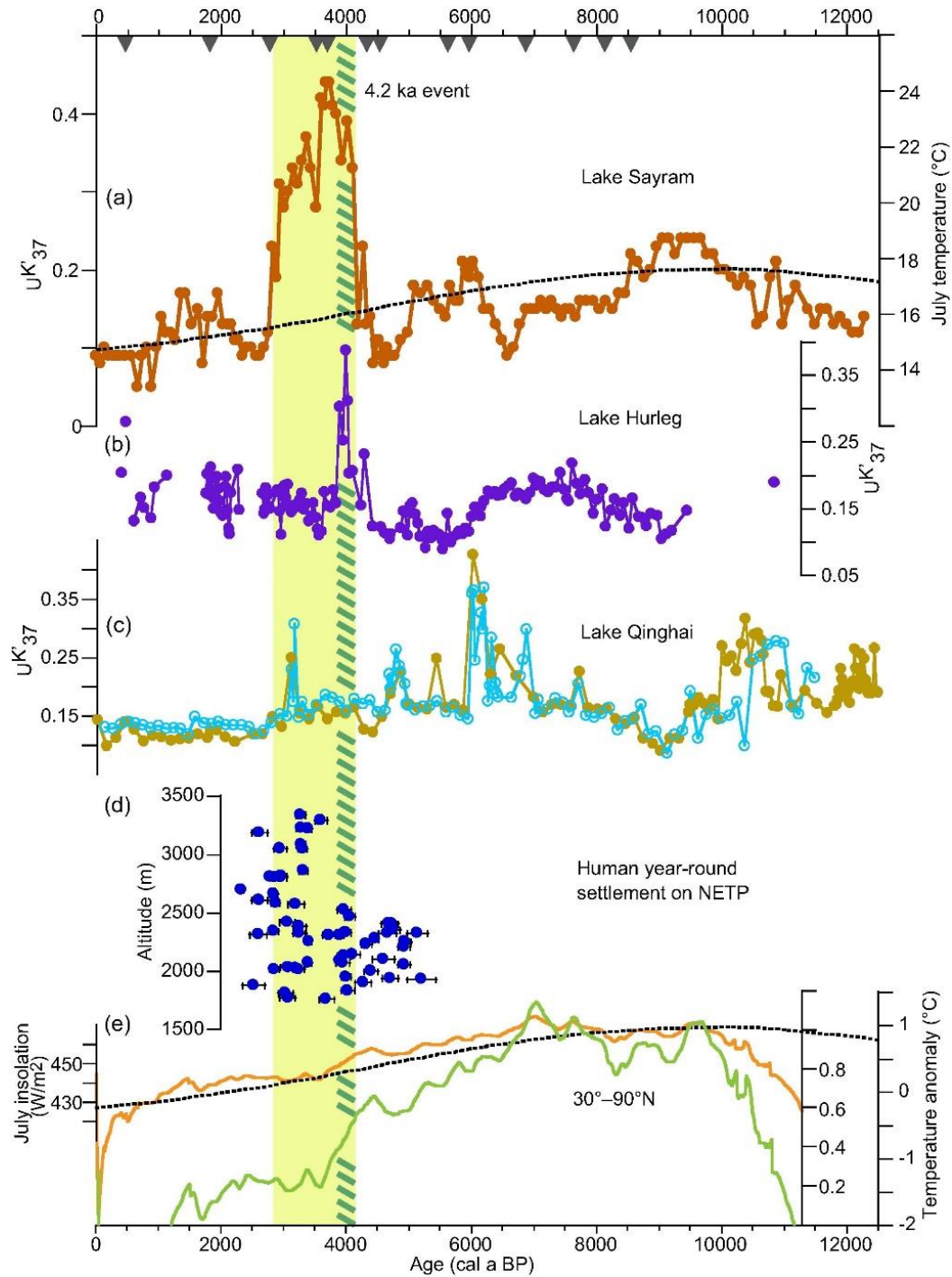


Figure 1. Holocene summer temperature records and human settlements in Northwest China. Alkenone U^K_{37} -temperature records from (a) Lake Sayram, with estimated July temperature; (b) Lake Hurleg [15]; and (c) Lake Qinghai [16], [17]. (d) Calibrated ^{14}C ages (with 2σ error bar indicated) of human year-round settlements on the northeastern Tibetan Plateau, NETP [12]. (e) Northern hemisphere extratropical temperature anomaly [1], its amplified view with negative anomaly cut off (light green), and superimposed $65^\circ N$ July insolation [35] (also in (a)). Triangles indicate ^{14}C dates at Lake Sayram. The exceptional warm interval and the cool/dry “4.2 ka event” [9] are highlighted.

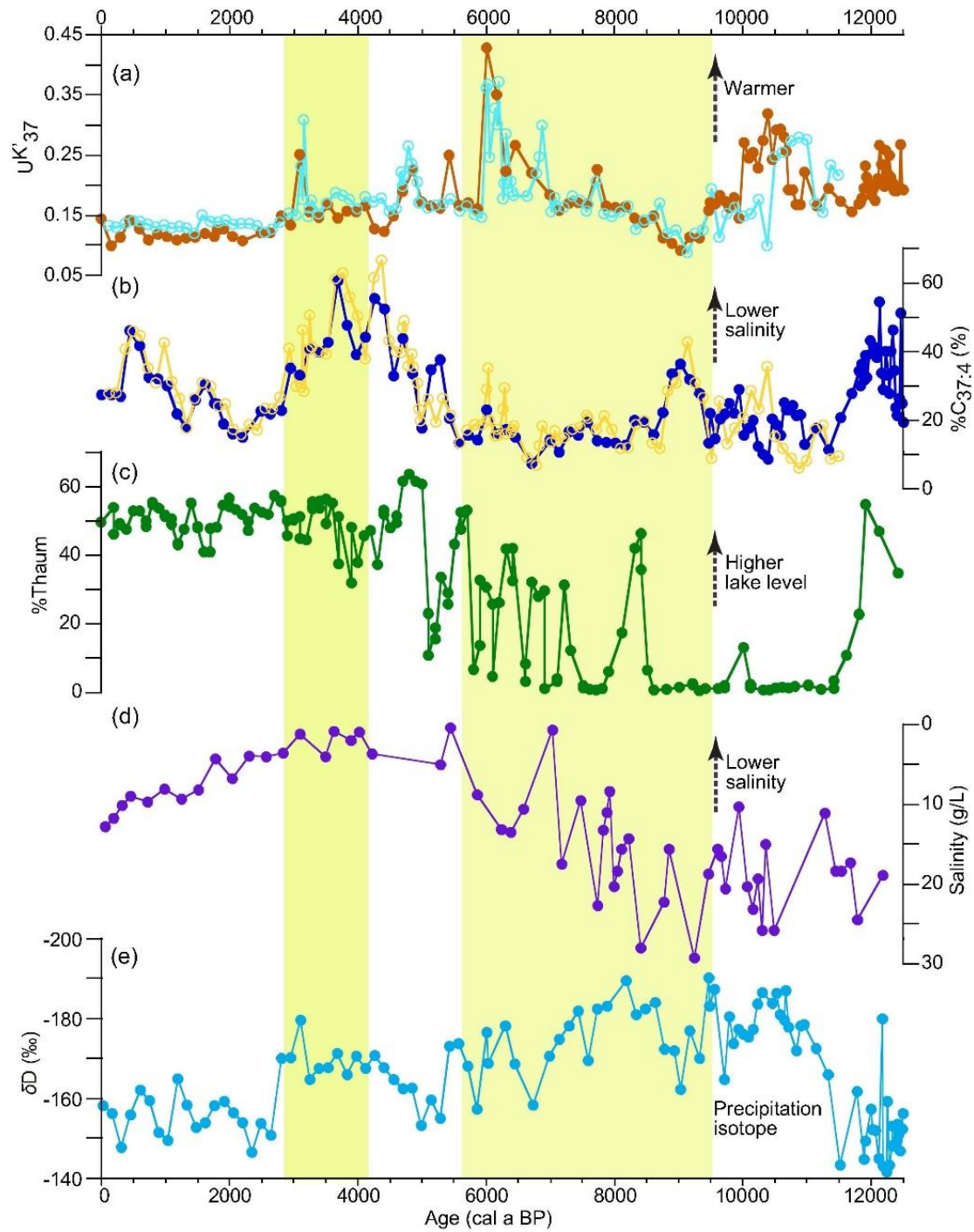


Figure 2. Holocene temperature, precipitation isotope and hydrological records from Lake Qinghai, China. (a) Updated $U^{K'_{37}}$ -temperature [16], [17]. (b) Salinity changes [16], [17] as indicated by the updated $\%C_{37:4}$. (c) Lake level changes as indicated by the percentage of thaumarchaeol in isoprenoid glycerol ethers ($\%Thaum$) [38]. (d) Reconstructed salinity based on ostracod Sr/Ca ratio [39]. (e) Hydrogen isotope (δD) of n-C28 fatty acid recording precipitation isotope [36]. The exceptional warm interval at 4200–2800 a BP, associated with wetter conditions at this lake, and interval of 9500–5500 a BP (warm mid- and early Holocene) are highlighted for comparison.

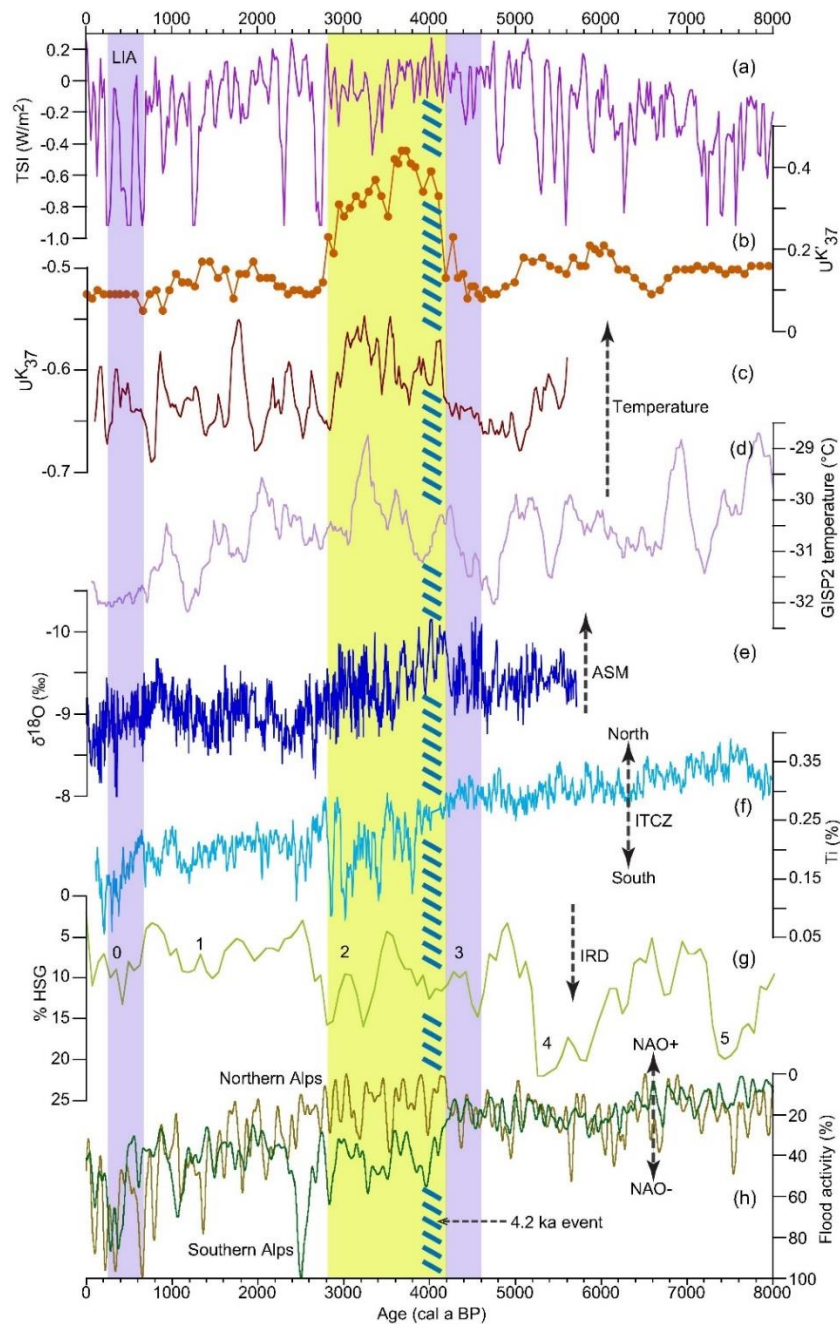


Figure 3. Global records showing climate anomalies at 4200–2800 a BP. (a) Solar activity [59] (TSI, total solar irradiance). (b) Lake Sayram temperature. (c) West Greenland temperature [42]. (d) Greenland ice core temperature (GISP2) [56]. (e) Speleothem $\delta^{18}\text{O}$ from the Sahiya Cave, India [14]. (f) Titanium content from the Cariaco Basin [58]. (g) Hematite-stained quartz grain (HSG) from North Atlantic, with “Bond Cycles” numbered [7]. (h) Flood activity in the Alps [57]. Intervals of 4200–2800 a BP, 4600–4200 a BP and LIA are highlighted. ASM: Asian summer monsoon; ITCZ: Intertropical Convergence Zone; IRD: ice-rafted debris; NAO: North Atlantic Oscillation.

5. 调和超大陆旋回模型与古俯冲带

翻译人：柳加波 liujb@sustech.edu.cn



Wolf J, Evans D A D. Reconciling supercontinent cycle models with ancient subduction zones [J]. Earth and Planetary Science Letters, 2021, 117293.

<https://doi.org/10.1016/j.epsl.2021.117293>

摘要：地幔最下层大型低剪切波速省（LLSVPs）的位置以及俯冲带的封闭环带，展示了地幔对流的长期模式。这些自盘古大陆解体以来一直稳定的结构，为锚定深时板块运动提供绝对参考系。关于超大陆旋回（内倾、外倾、正倾）的简单概念模型预测了全球俯冲带和可能的 LLSVP 点位。我们开发了一种工具，能够在统计上对比理想化的超大陆循环模型与古地理重建的全球俯冲带古纬度分布。LLSVP 周围的理想化环带能够较好的解释晚于 250 Ma 的俯冲带位置，但是更可靠的概念模型必须要考虑环带内特提斯的轨迹或者“臂”。在 540 到 250 Ma 之间，与古地理的强相关性不需要这样的正交臂来；但全球俯冲环带逐渐旋转了约 90°。我们的研究表明，行星二阶地幔结构是持续的，但不是永恒的：从一个超大陆周期到下一个超大陆周期，它们重新调整了自己的绝对位置。

ABSTRACT: Long-term patterns of mantle convection are illustrated by the locations of large low-shear-velocity provinces (LLSVPs) in the lowermost mantle, as well as an enclosing girdle of subduction zones. These structures, stable since Pangea's breakup, have been proposed to provide an absolute reference frame to anchor plate motions in deep time. Simple conceptual models of the supercontinent cycle (introversion, extroversion, orthoversion) predict differing loci of global subduction zones and inferred LLSVPs. We develop a tool to statistically compare idealized supercontinent cycle models with paleolatitude distributions of global subduction zones from paleogeographic reconstructions. We find that subduction zone locations younger than 250 Ma are moderately well described by an idealized girdle around the LLSVPs, but more robust conceptual models must take into account a Tethyan locus or “arm” within the girdle. Between 540 and 250 Ma, such an orthogonal arm is not needed to generate robust correlations with paleogeography; but the global subduction girdle is found to rotate progressively by approximately 90°. Our results

suggest that planetary degree-two mantle structures are long-lived but not eternal: they reorganize their absolute locations from one supercontinent cycle to the next.

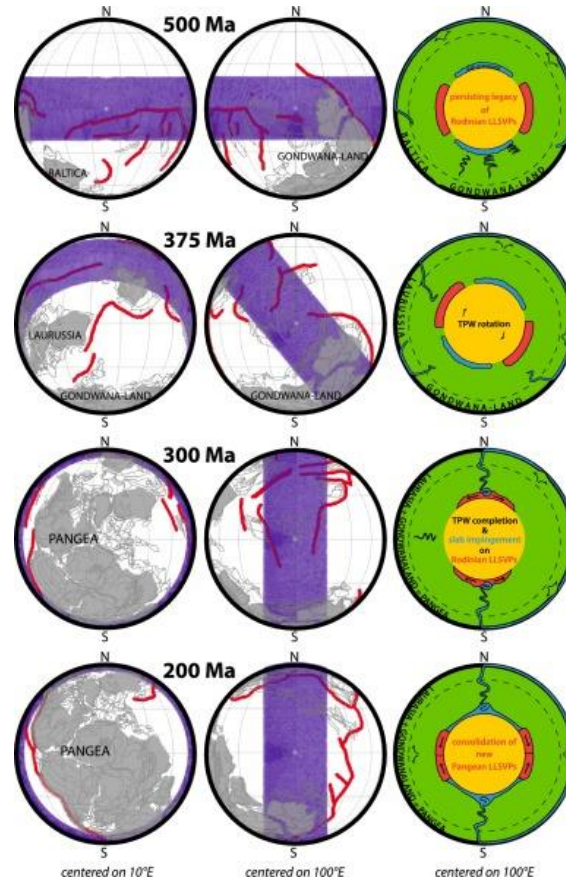


Figure 1. Schematic illustration of the proposed orthoversion model at four time steps. The left and center columns (centered on 10°E and 100°E, respectively) show surface patterns of subduction zones (red) taken from Merdith et al. (2020); a corresponding best-fit synthetic girdle is shown in violet. The right column schematically presents whole-Earth cross-sections from the same time intervals, with subducting slabs and slab graveyards (blue) and LLSVP material (red). At 500 Ma (first row), Gondwana-Land lies at the South Pole, surrounded by an equatorial girdle of young subduction zones that do not yet extend into the lower mantle. By 375 Ma (second row), slabs have sunken into the lower mantle and initiated true polar wander. This rotation is complete by 300 Ma (third row) with attainment of a meridional subduction girdle. The subducting slabs impinge upon and disaggregate the relict Rodinian LLSVPs, ultimately leading to the reconstitution of new Pangean LLSVPs by 200 Ma (fourth row).

6. 地幔柱和其在地球过程中的作用



翻译人:李园洁 liyj3@sustech.edu.cn

Koppers A A P, Becker T W, Jackson M G, et al. Mantle plumes and their role in Earth processes [J]. Nat Rev Earth Environ, 2021, 2, 382–401.

<https://doi.org/10.1038/s43017-021-00168-6>

摘要: 1970 年代第一次提出地幔柱用来解释板内热点火山，但是由于地球物理成像分辨地幔上升仍存在困难，地球化学和地质年代学数据的解释存在分歧，地幔柱的来源、动力学和成分以及它们与板块构造的联系仍有争议。本篇综述中，我们讨论地震层析成像、地幔流模型、板块构造重建和地球化学分析的进展，获得对地幔柱更详细的了解。观测结果表明地幔柱同时具有热和化学性质，能够维持复杂宽大的形状，至少 18 个地幔柱起源于地幔底部区域。深部地幔柱起源得到热点火山的地球化学的证实，其可提供的证据包括深部循环的俯冲成分的夹带，原始地幔域和可能来自地核的物质。深部地幔柱通常因大尺度地幔流动而偏转，导致热点运动，以解决过去的板块构造运动。未来的研究需要提高地震层析成像的分辨率以便小于 100 km 尺度上显示深部地幔柱的结构。仍需要综合多指标地球化学和定年数据更好地解决地幔柱的时空和化学演化过程。

ABSTRACT: The existence of mantle plumes was first proposed in the 1970s to explain intra-plate, hotspot volcanism, yet owing to difficulties in resolving mantle upwellings with geophysical images and discrepancies in interpretations of geochemical and geochronological data, the origin, dynamics and composition of plumes and their links to plate tectonics are still contested. In this Review, we discuss progress in seismic imaging, mantle flow modelling, plate tectonic reconstructions and geochemical analyses that have led to a more detailed understanding of mantle plumes. Observations suggest plumes could be both thermal and chemical in nature, can attain complex and broad shapes, and that more than 18 plumes might be rooted in regions of the lowermost mantle. The case for a deep mantle origin is strengthened by the geochemistry of hotspot volcanoes that provide evidence for entrainment of deeply recycled subducted components,

primordial mantle domains and, potentially, materials from Earth’s core. Deep mantle plumes often appear deflected by large-scale mantle flow, resulting in hotspot motions required to resolve past tectonic plate motions. Future research requires improvements in resolution of seismic tomography to better visualize deep mantle plume structures at smaller than 100-km scales. Concerted multi-proxy geochemical and dating efforts are also needed to better resolve spatiotemporal and chemical evolutions of long-lived mantle plumes.

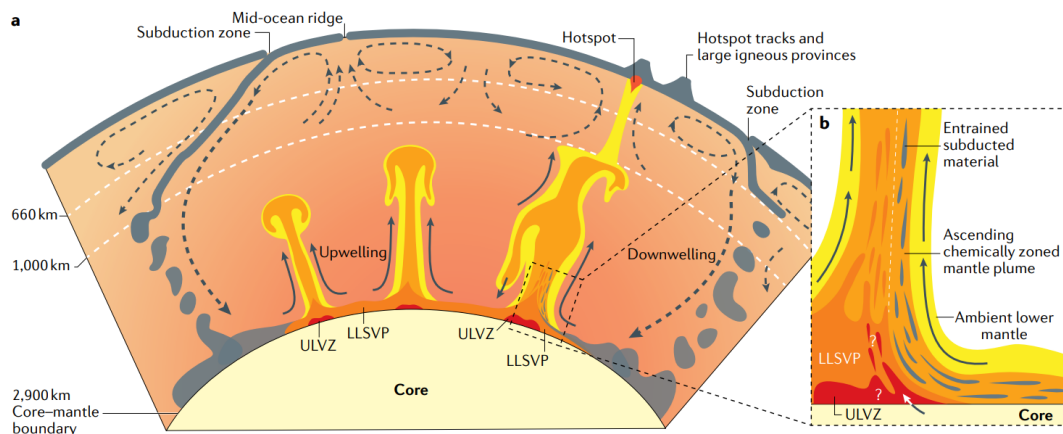


Figure 1. Dynamic nature of Earth’s interior. a | Schematic cross section through Earth’s interior, depicting the key components of plume generation and upwelling near, above and along the edges of a large low-shear-velocity province (LLSVP) and near the core–mantle boundary. These LLSVPs might contain localized ultra-low velocity zones (ULVZs) and along their edges subducted material may pile up over hundreds of millions of years. b | Schematic cross section of a plume root showing the entrainment of subducted materials, LLSVP and ULVZ components, and possibly core materials at the edge of a LLSVP and centred above an ULVZ (that might be a unique deep mantle locality containing partial melt).

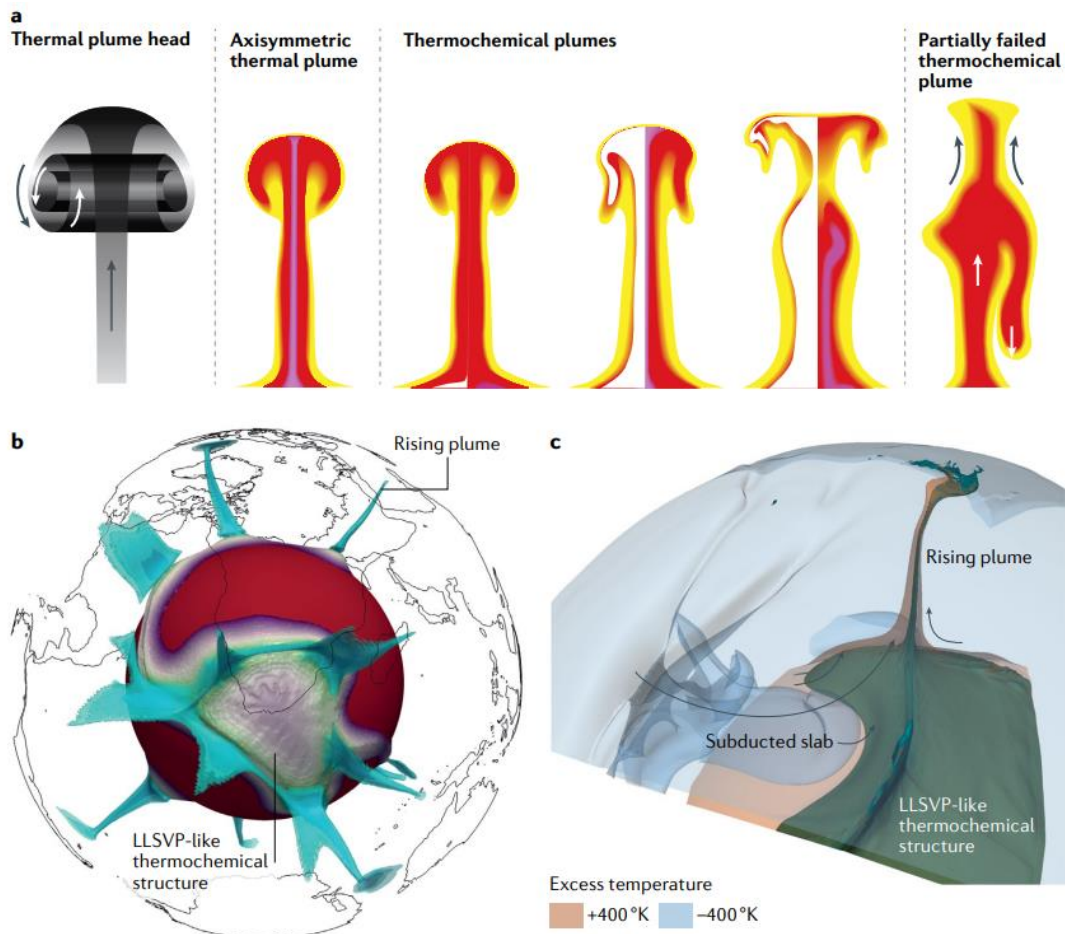


Figure 2. Examples of rising thermal and thermochemical plumes. a | Representations of rising thermal plume head models: a thermal plume head connected by a stem to the source region; an axisymmetric thermal plume; three thermochemical plumes with colours representing temperature differences (purple/red = hottest; orange = cooler; yellow = coolest; white = chemically different plume material); and, finally, a model of a plume that partially fails when entrained materials (that are too heavy) collapse in the top of the conduit (based on laboratory syrup tank experiments). b | 3D and time-dependent numerical model with plumes (blue) rising from a large low-shear-velocity province (LLSVP) situated below southern Africa. c | 3D model showing rising plumes from the LLSVP margins that are substantially hotter than the surrounding lowermost mantle, with large temperature anomalies of about 500K. Panel b adapted with permission from ref.13, Wiley, © 2015. American Geophysical Union. All Rights Reserved. Panel c adapted with permission from ref.77, Proceedings of the National Academy of Sciences.

7. 古新世/始新世期间火山活动驱动的碳反馈



翻译人：蒋晓东 jiangxd@sustech.edu.cn

Kender S, Bogus K, Pedersen G K, et al. Paleocene/Eocene carbon feedbacks triggered by volcanic activity[J]. Nature Communications, 2021, 12, 5186.

<https://doi.org/10.1038/s41467-021-25536-0>

摘要：古新世-始新世极热时段（PETM）是发生在约 56 Ma 前的一次碳释放和全球快速升温事件。尽管模型证据和露头、指标记录表明这一时期火山碳释放，但还是不能识别出 PETM 的驱动机制，或者是否涉及了多个碳储库。本研究对取自北海的沉积物进行研究，提供了优化的火山指标 Hg/TOC，结果表明在 PETM 之前和发生时期均具有来北大西洋火山岩省的显著的火山脉冲，这很可能驱动了或者维持了 CO₂ 释放。然而 PETM 开始时对应于一次 Hg 的低值，这意味着至少有另一个碳源释放了大量温室气体引起初始的暖化。我们的结果支持地球系统中存在“引爆”法则，这驱动了额外的碳释放，并且驱动了地球气候向温室转变。

ABSTRACT: The Paleocene–Eocene Thermal Maximum (PETM) was a period of geologically-rapid carbon release and global warming ~56 million years ago. Although modelling, outcrop and proxy records suggest volcanic carbon release occurred, it has not yet been possible to identify the PETM trigger, or if multiple reservoirs of carbon were involved. Here we report elevated levels of mercury relative to organic carbon—a proxy for volcanism—directly preceding and within the early PETM from two North Sea sedimentary cores, signifying pulsed volcanism from the North Atlantic Igneous Province likely provided the trigger and subsequently sustained elevated CO₂. However, the PETM onset coincides with a mercury low, suggesting at least one other carbon reservoir released significant greenhouse gases in response to initial warming. Our results support the existence of ‘tipping points’ in the Earth system, which can trigger release of additional carbon reservoirs and drive Earth’s climate into a hotter state.

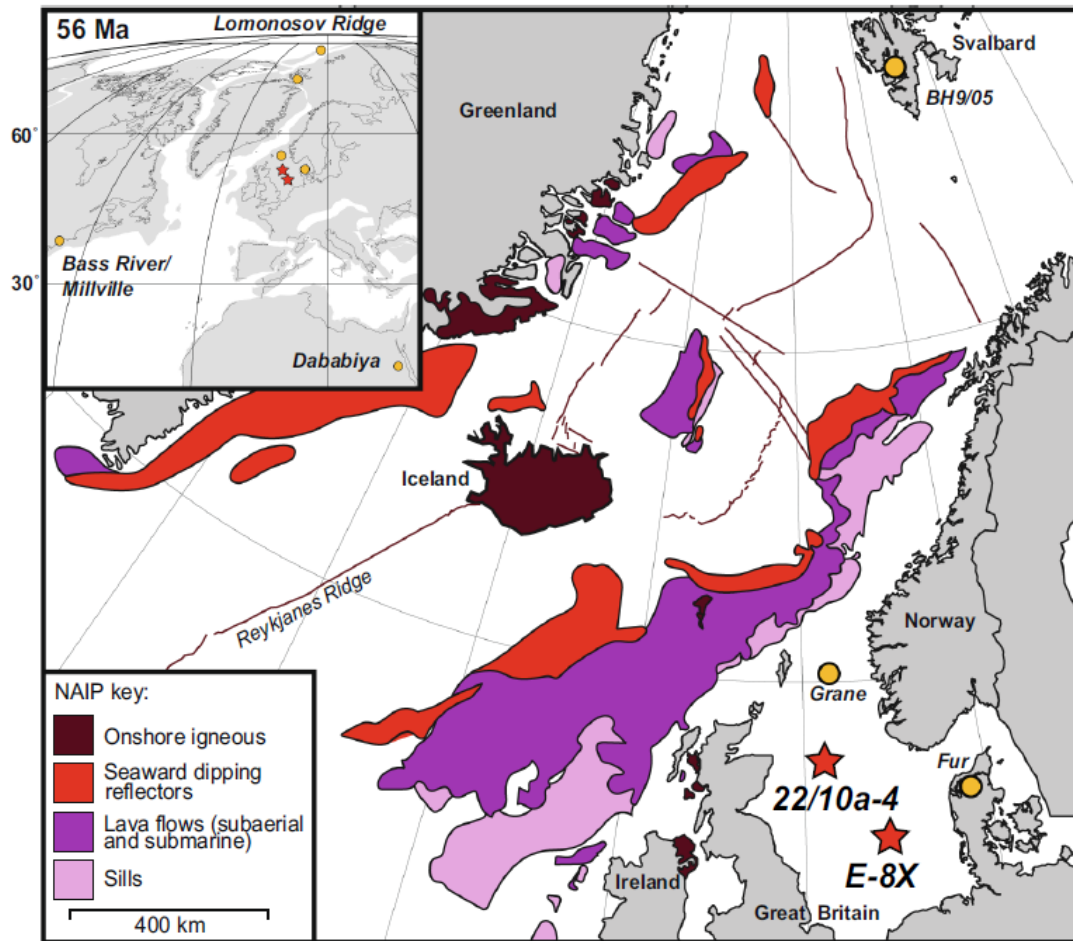


Figure 1. Location maps of the North Atlantic Igneous Province (NAIP) and sediment cores sites analysed in this study. The simplified NAIP main map shows the estimated ranges of its various components. ‘Seaward dipping reflectors’ are well-defined seismic reflectors beneath the uppermost basalt, interpreted as large subaerial sheet lava flows associated with rifting. Other lava flows are thought to be a combination of subaerial and submarine, and sills were considered as intruded into the upper crust. The insert map is a Mollweid projection of modern continents (lines) on a palaeogeographic reconstruction, generated from, of continental plates (grey) centred at 56 Ma

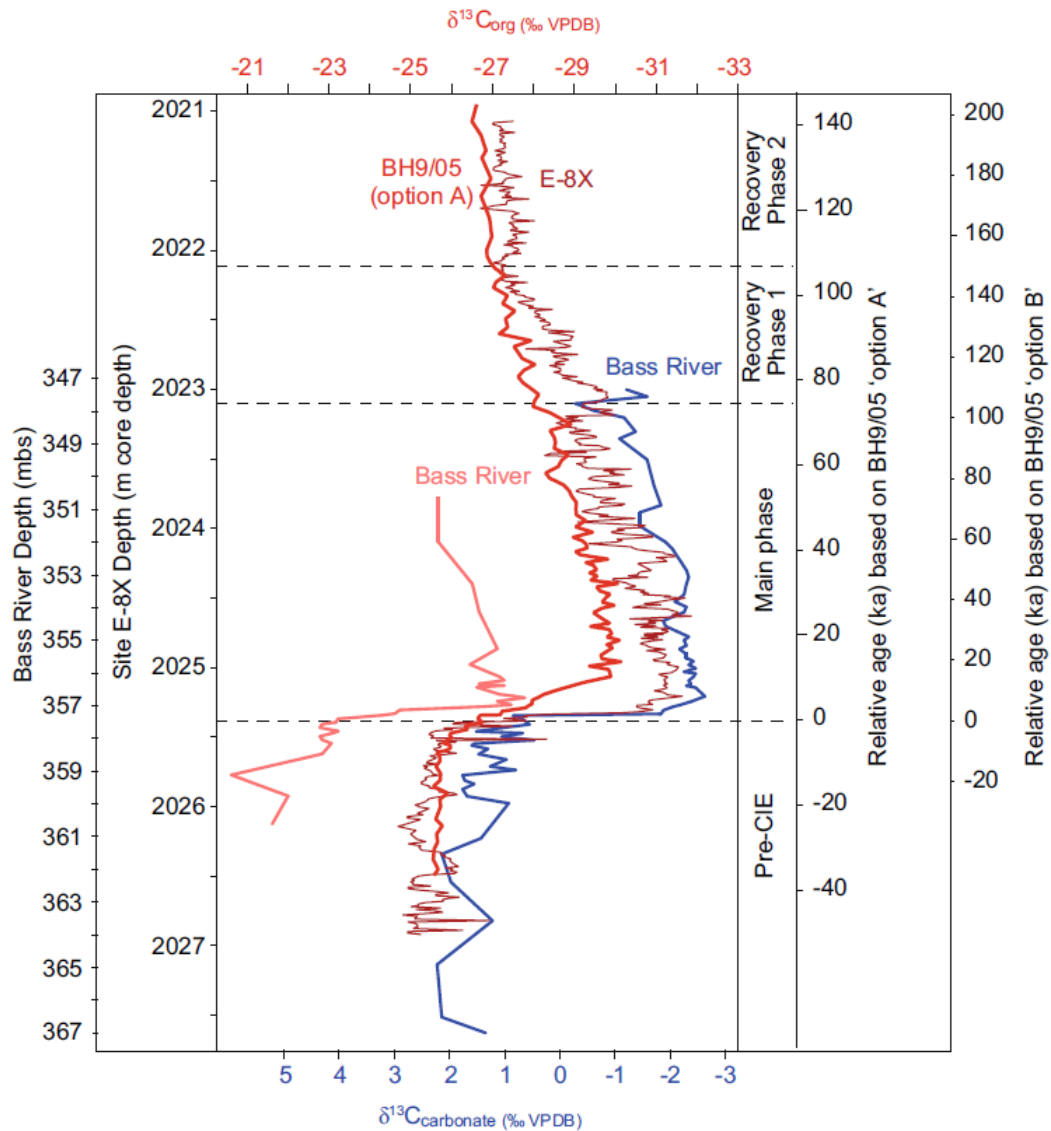


Figure 2. Carbon isotope correlation of two sites with Svalbard core BH9/05. The $\delta^{13}C$ of both organic carbon ($\delta^{13}C_{org}$) and inorganic carbonate ($\delta^{13}C_{carbonate}$) from North Sea well site E-8X (this study) and Bass River, are correlated to Svalbard core BH9/05 based on the overall shape of the records, with particular emphasis on the carbon isotope excursion (CIE) inflection points during the rapid onset and gradual recovery phases. The relative age model is based on two proposed solutions for cyclostratigraphy of core BH9/05. Bass River core depth in metres below the surface (mbs).

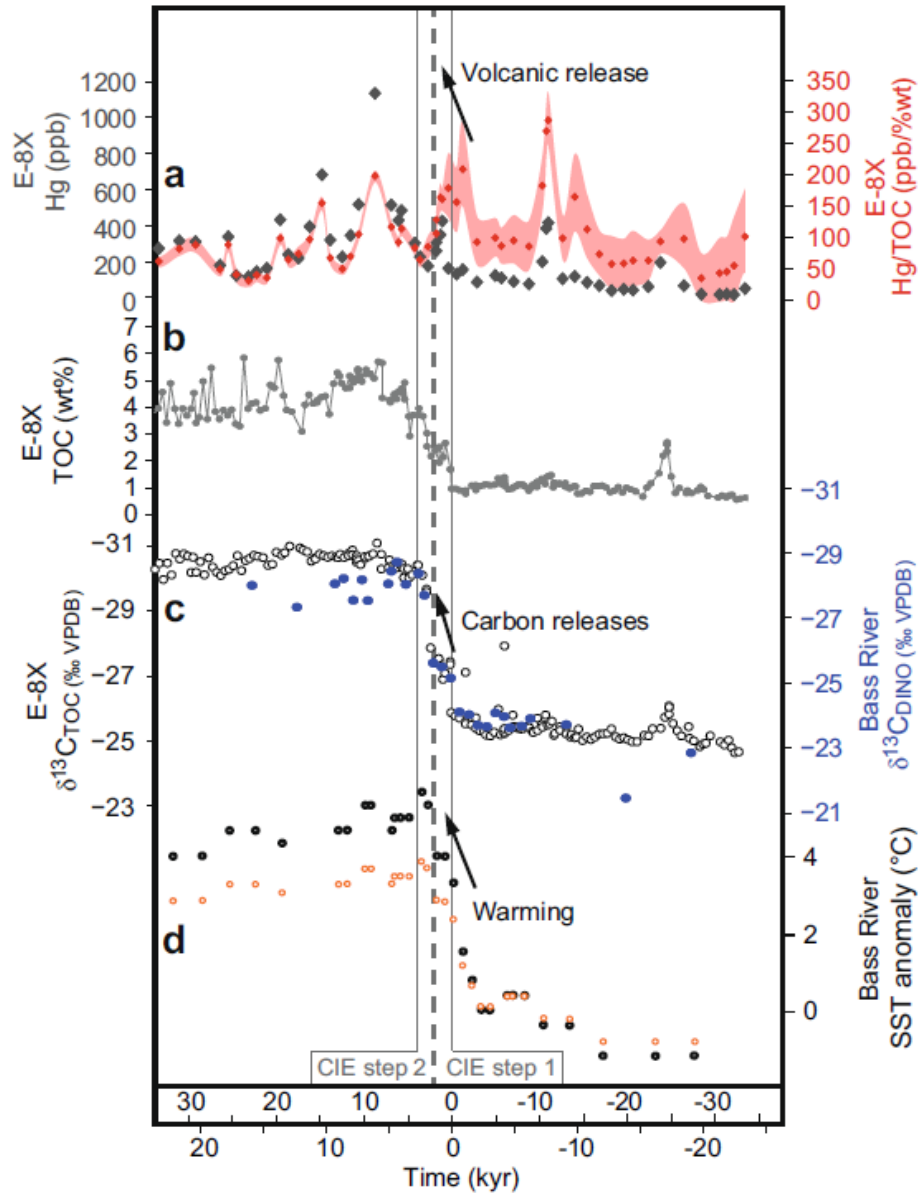


Figure 3. Proxies for volcanism, carbon release and temperature in the time domain; thousands of years from the start of the PETM carbon isotope excursion (CIE). a Sedimentary mercury (Hg) and Hg/total organic carbon (Hg/TOC) for core E-8X (this study). Hg/TOC envelope reflects an analytical error, illustrating higher uncertainty in samples with lower TOC. B Sedimentary TOC weight (wt) % for core E-8X (this study). c Sediment proxy records for TOC isotopes ($\delta^{13}\text{C}_{\text{TOC}}$) at E-8X (this study), and carbon isotopes of sedimentary organic-walled dinoflagellate cysts ($\delta^{13}\text{C}_{\text{DINO}}$) from Bass River, New Jersey, used to correlate the two sites. d Sea surface temperature (SST) anomaly proxy data from Bass River, New Jersey. The same data are presented with two different calibrations for temperature in orange and black.

8. 纳米流动与地震不稳定性



翻译人：周洋 zhouy3@sustech.edu.cn

Sun Hongyu, Matej Pec. *Nanometric flow and earthquake instability* [J]. *Nature Communications*, 2021, 12, 6779.

<https://doi.org/10.1038/s41467-021-26996-0>

摘要: 断层带形成于构造块体之间的相对运动并控制着地震能量。断层岩中的纳米颗粒在“主滑移带”中无处不在，这些颗粒决定了断层的稳定性。然而，断层岩纳米颗粒的流变学仍然缺乏约束。我们发现，当在相同的实验条件下变形时，断层岩比它们的微晶弱一个数量级。因此断层岩的弱化是内在的，当纳米颗粒形成时发生弱化。然而，由于测得的应力指数 n 为 1.3 ± 0.4 ，很难产生“速率减弱”行为，活化能 Q 较低，为 $16,000 \pm 14,000$ J/mol，这意味着材料将具有很强的“速率增强”特征，对温度敏感性弱。然而，一旦这些薄弱层在运动有利的网络中合并，断层带就会被破坏。这种类型的不稳定性不同于地壳地震的摩擦不稳定性。

ABSTRACT: Fault zones accommodate relative motion between tectonic blocks and control earthquake nucleation. Nanocrystalline fault rocks are ubiquitous in “principal slip zones” indicating that these materials are determining fault stability. However, the rheology of nanocrystalline fault rocks remains poorly constrained. Here, we show that such fault rocks are an order of magnitude weaker than their microcrystalline counterparts when deformed at identical experimental conditions. Weakening of the fault rocks is hence intrinsic, it occurs once nanocrystalline layers form. However, it is difficult to produce “rate weakening” behavior due to the low measured stress exponent, n , of 1.3 ± 0.4 and the low activation energy, Q , of $16,000 \pm 14,000$ J/mol implying that the material will be strongly “rate strengthening” with a weak temperature sensitivity. Failure of the fault zone nevertheless occurs once these weak layers coalesce in a kinematically favored network. This type of instability is distinct from the frictional instability used to describe crustal earthquakes..

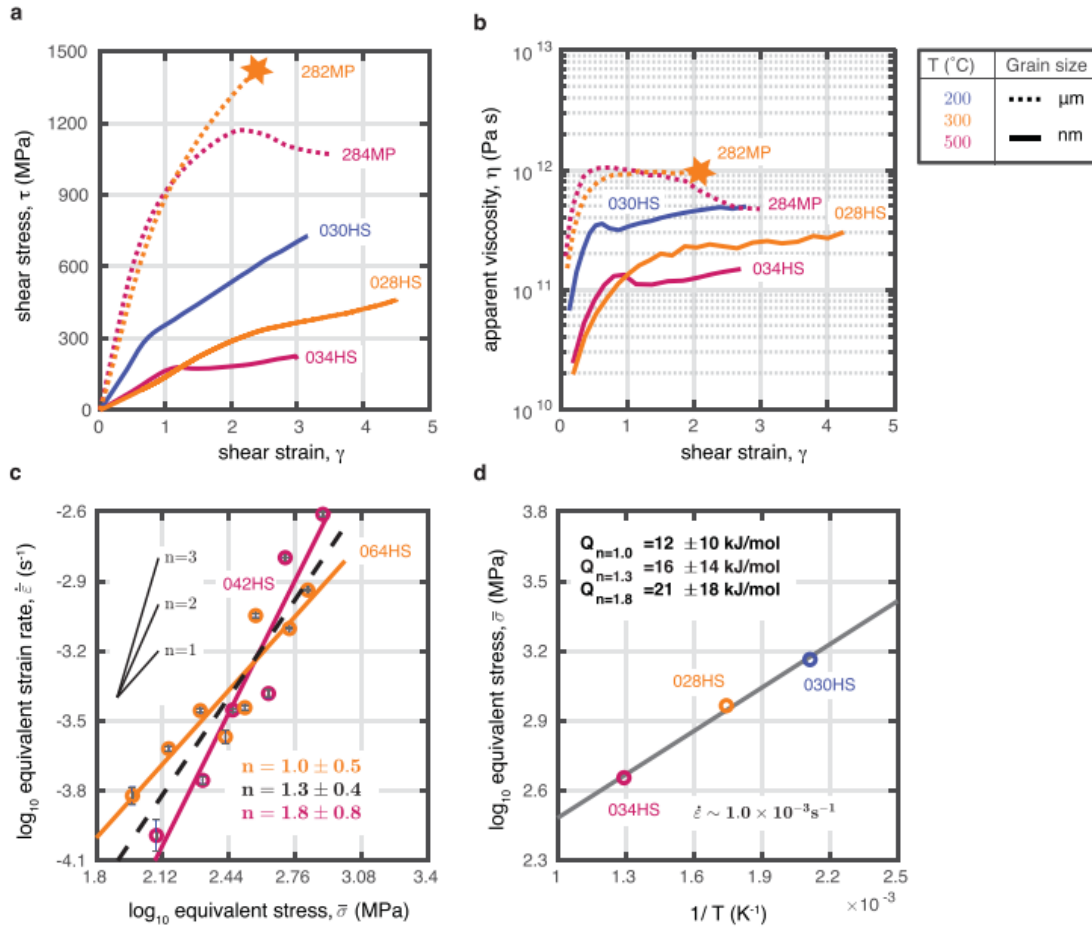


Figure 1. Mechanical data. a Comparison of the shear strength between nanocrystalline fault rocks, $\sim 0.1 \mu\text{m}$, and microcrystalline fault rocks, $\leq 200 \mu\text{m}$. The nanocrystalline fault rocks are about 1 GPa weaker than the microcrystalline ones. b Nanocrystalline fault rocks have about an order of magnitude lower apparent viscosity than the microcrystalline fault rocks at same T. c Determination of the stress exponent, $n = 1.3 \pm 0.4$. The blue error bars on the plot represent the standard deviation of measurements. The stress exponent is estimated by fitting to data from both experiments, given that the activation energy of the material is low. d Arrhenius plot determining the activation energy using the constant-displacement-rate experiments. For details of conversion from shear to equivalent stresses and strains see the “Methods” section.

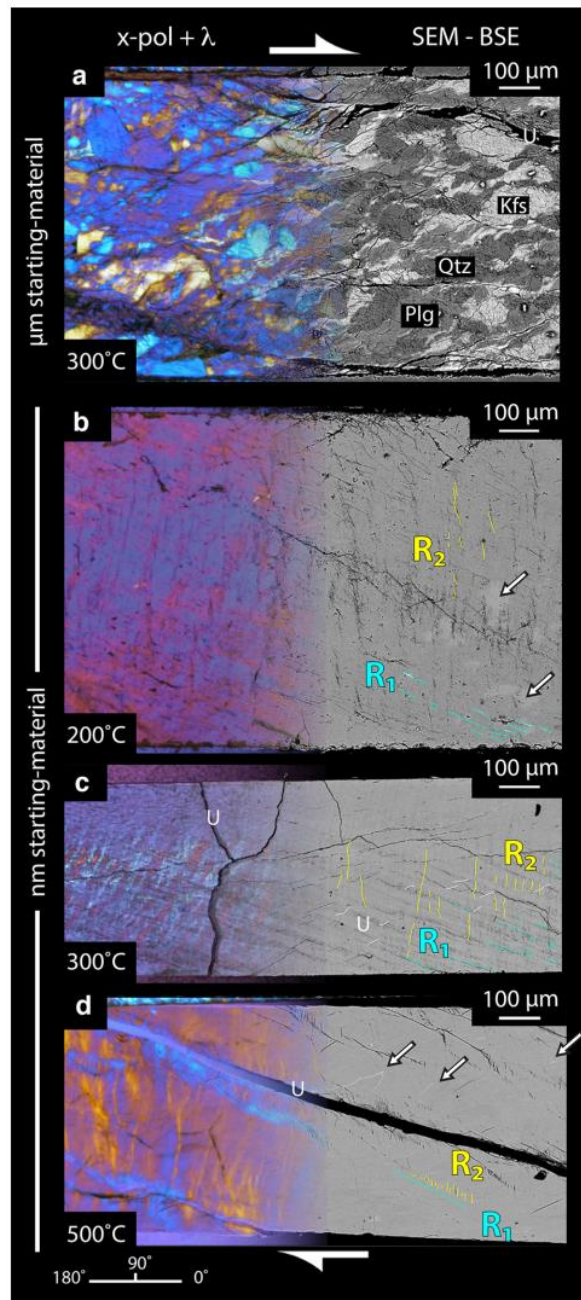


Figure 2. Microstructural observations of the sheared fault rocks in polarized light (left) and SEM-BSE (right). Kfs - potassium feldspar, Qtz - quartz, Plg - plagioclase, U - unloading cracks. R1 & R2 - Riedel shears. Angle convention shown in the lower left. a Microcrystalline fault rocks. b Nanocrystalline fault rocks deformed at 200 °C. Note pervasive R1 and R2 fractures and locally brighter material in BSE z-contrast indicating different chemical composition and/or density (arrows) c Nanocrystalline fault rocks deformed at 300 °C, note alternating cyan/orange layers highlighting kinkbands in the optical image. d Nanocrystalline fault rocks deformed at 500 °C. Arrows indicate stretched layers and smeared out domains indicative of continuous flow.

9. 喜马拉雅 Sikkim 褶皱逆断层带磁组构与应变组构的运动学方法



翻译人：张琪 zhangq7@sustech.edu.cn

Das J, Bhattacharyya K, Mantani M, A kinematic approach for investigating magnetic and strain fabrics from constrictional and flattening domains of shear zones in Sikkim Himalayan fold thrust belt [J]. Journal of Structural Geology, 2021, 149, 104388.

<https://doi.org/10.1016/j.jsg.2021.104388>

摘要：本文研究了喜马拉雅 Sikkim 主要剪切带 Pelling - Mungsiari 逆断层(PT)的磁组构、糜棱组构与应变组构之间的关系，这些信息记录了沿其输运方向不同的糜棱组构与应变几何结构。主要露头显示由扁平椭球体的 SL -构造转变为局部细长椭球体的 L-构造，形成向型飞来峰。磁组构与 PT 变形有关，并受飞来峰局部褶皱作用的影响。磁性颗粒和拉伸矿物线理的方位变化大于平面组构的走向。不论其应变几何形状如何，大多数断层岩包括构造上覆主中央冲断层的 SL 糜棱岩，都记录为磁化率扁平椭球体。顺磁组分记录了一个增量变形阶段，在最内陆的断层岩中冻结为扁平化磁化率椭球体，并没有被连续的更高量级的收缩应变重新排列，并伴有局部的侧段破，此外，石英颗粒之间的应变分配、追踪有限应变组构和云母对磁组构的主要贡献解释了断层岩中组构的偏差。

ABSTRACT: We investigate the relationships among magnetic, mylonitic and strain fabrics from the Pelling-Mungsiari thrust (PT), a major shear zone in the Sikkim Himalaya, that records varying mylonitic fabrics and strain geometry along its transport direction. The fabric changes from an SL-tectonite with oblate strain ellipsoids in its main exposures, to a local, transport-parallel L-tectonite with prolate strain ellipsoids, forming a synformal klippen. Magnetic fabric is related to the PT deformation, and is affected by the local folding of the klippen. The bearings of magnetic and stretching mineral lineation vary more than the orientations of the planar fabrics. Irrespective of their strain geometry, most of the fault rocks, including SL mylonites of the structurally overlying Main Central thrust, record oblate susceptibility ellipsoids. The paramagnetic phases tracked an incremental deformation stage that froze as oblate susceptibility ellipsoid in the hinterlandmost fault rocks, and was not realigned by successive higher magnitude,

constrictional strain, associated with a local, lateral ramp, followed by flattening strain in the forelandmost exposure during translation of the PT. Additionally, strain partitioning between quartz, tracking the finite strain fabric, and micas primarily contributing to the magnetic fabric explain the deviations in the studied fabrics in the fault rocks.

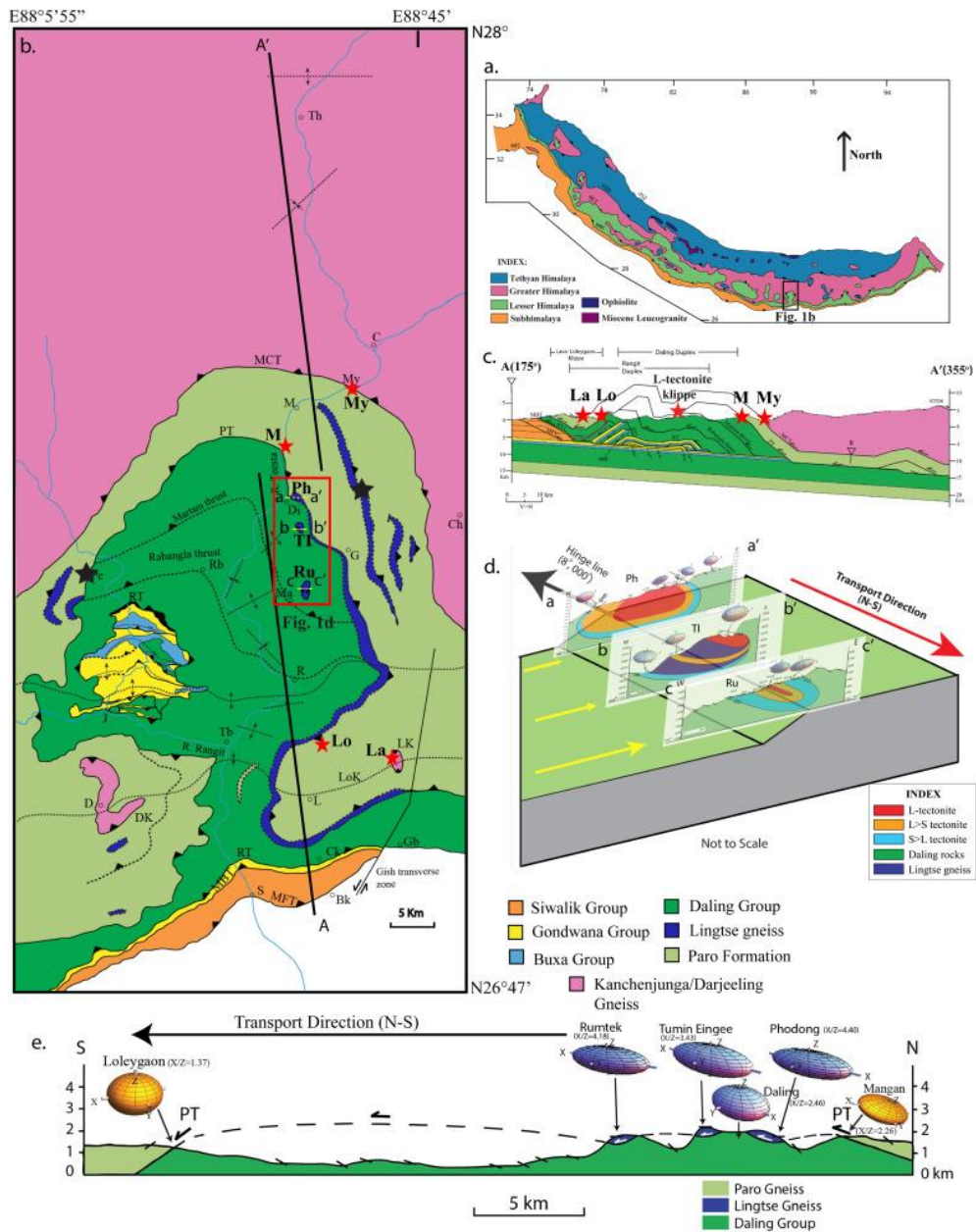


Figure 1. (a) Geological map of the Himalayan FTB (modified after Yin, 2006) showing the location of the Sikkim Himalaya (marked as black box). (b) Regional geologic map of the Sikkim Himalayan FTB (modified after Roy, 1976; Bhattacharyya and Mitra, 2009; Bhattacharyya et al., 2015a). Black stars represent the location of the Lingtse gneiss protolith and red stars represent the

studied locations of PT and MCT zones. Red box marks the linear, discontinuous L-tectonite klippe. (c) Transport-parallel regional balanced cross-section along the A-A' transect from the eastern Sikkim Himalaya (Parui and Bhattacharyya, 2018) showing the studied main exposures of the PT and MCT zones using the red stars. (d) Sub-PT lateral ramp model along with transport-perpendicular cross-sections for the three discontinuous L-tectonite mylonite klippe: Phodong mylonite zone (a-a'), Tumin Eingee mylonite zone (b-b') and Rumtek mylonite zone (c-c') that lie east of A-A'. Please note the three mylonite zones are folded with their hinge lines trending N. The strongest (Roy, 1976) linear fabric is restricted to the hinge zone and is spatially associated with the $L > S$ and $S > L$ fabrics within its limbs (modified from Das et al., 2016). (e) Cross-section along the transport direction (N-S) showing locations of L-tectonite klippen and the associated prolate strain ellipsoids (Bhattacharyya et al., 2015a), and Mangan PT zone in the hinterland and Loleygaon PT zone in the foreland with the corresponding oblate strain ellipsoids. MCT: Main Central thrust; PT: Pelling thrust; RT: Rangarh thrust; MBT: Main Boundary thrust; MFT: Main Frontal thrust; DK: Darjeeling klippe; LK: Lava Klippe; LOK: Loleygaon Klippe; LTK: L-tectonite klippen; RD: Rangit duplex. Bk– Bagrakote, C– Chungthang, Ch- Changu lake, Ck- Chuikhim village, D– Darjeeling, Di– Dikchu, G- Gangtok, Gb- Gorubathan, J- Jorethang, L- Loleygaon, M– Mangan, Ma- Martam, My- Mayang Chu, Pe– Pelling, R- Rangpo, Rb- Rabangla, Rd- Rangit duplex, S-Sevoke, Tb- Teestabazar, Th- Thangu.

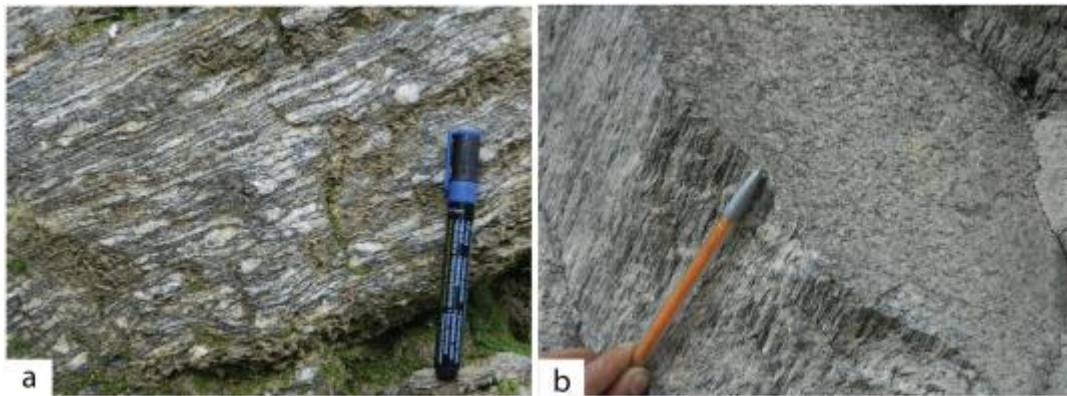


Figure 2. (a) An SL mylonite from the main exposures of the PT where the foliation is defined by quartz, feldspar and biotite, muscovite. (b) The PT fault rock forming an L-tectonite in the Phodong mylonite klippe. The linear fabric is defined by stretched biotite, quartz.

10. 中生代以来以大陆岛弧为主的全球化学风化作用

翻译人：王敦繁 Dunfan-w@foxmail.com



Gernon T, Hincks T, Merdith A, et al. *Global chemical weathering dominated by continental arcs since the mid-Paleozoic* [J]. *Nature Geoscience*, 2021, 14:690-696.

<https://doi.org/10.1038/s41561-021-00806-0>

摘要：地球板块构造活动通过火山排气和硅酸盐岩石风化作用调节碳循环，进而调节气候。造山活动、岛弧-大陆碰撞和热带大陆聚集都被认为在控制全球的风化通量，岛弧活动也是大气中二氧化碳的主要贡献者。然而，这些过程在很大程度上是孤立地考虑的，而实际上它们都是紧密耦合的。为了恰当地解释这些过程之间的相互作用，以及在地球系统中存在的固有的数百万年滞后，我们需要描述它们复杂的相互依赖关系。在这里，我们利用贝叶斯网络分析了过去4亿年这些相互依赖关系，以确定全球化学风化信号的主要关系、时间滞后和驱动因素。我们发现大陆火山弧的长度——地球上侵蚀速度最快的构造活动——对全球化学风化通量的控制最强。我们提出，二氧化碳的快速下降和岛弧活动相关，并且稳定了地质时期的地表温度，这与普遍认为的这种稳定性主要是通过海底和大陆内部风化之间的微妙平衡来实现的观点相反。

ABSTRACT: Earth's plate-tectonic activity regulates the carbon cycle and, hence, climate, via volcanic outgassing and silicate-rock weathering. Mountain building, arc-continent collisions and clustering of continents in the tropics have all been invoked as controlling the weathering flux, with arcs also acting as a major contributor of carbon dioxide to the atmosphere. However, these processes have largely been considered in isolation when in reality they are all tightly coupled. To properly account for interactions among these processes, and the inherent multi-million-year time lags at play in the Earth system, we need to characterize their complex interdependencies. Here we analysis these interdependencies over the past 400 million years using a Bayesian network to identify primary relationships, time lags and drivers of the global chemical weathering signal. We find that the length of continental volcanic arcs—the fastest-eroding surface features on Earth—exerts the strongest control on global chemical weathering fluxes. We propose that the

rapid drawdown of carbon dioxide tied to arc weathering stabilizes surface temperatures over geological time, contrary to the widely held view that this stability is achieved mainly by a delicate balance between weathering of the seafloor and the continental interiors.

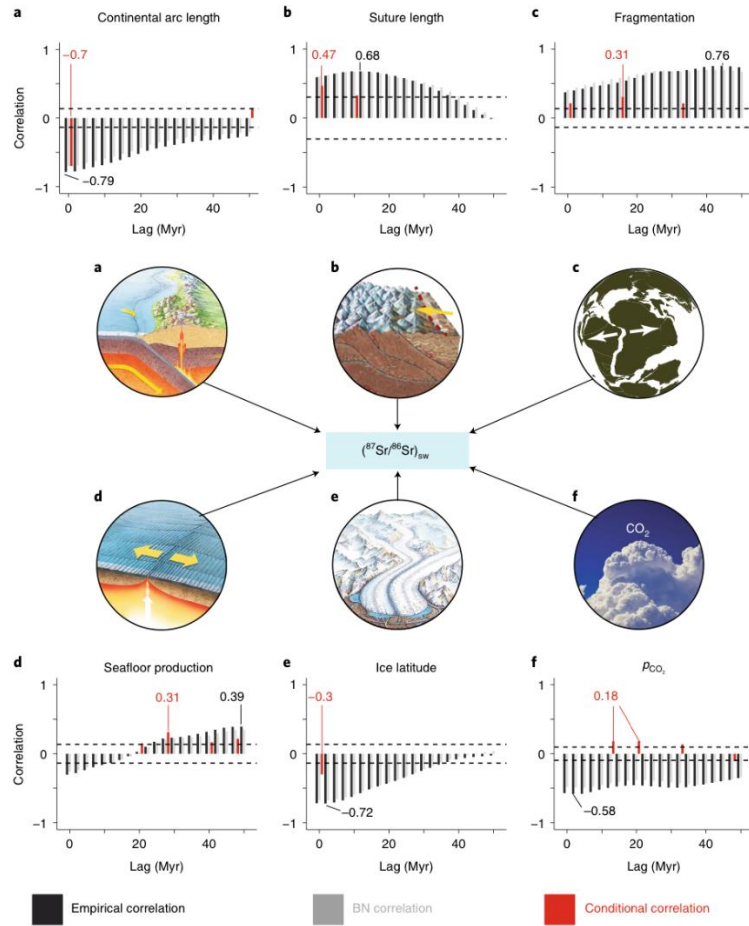


Figure 1. Simplified network showing key geological processes and correlations with seawater Sr.

11. 二叠纪、三叠纪地磁场长期变化及对古地磁场特征的指示



翻译人：张伟杰 12031188@mail.sustech.edu.cn

Handford B T, Biggin A J, Haldan M M, et al. *Analysing Triassic and Permian Geomagnetic Palaeosecular Variation and the Implications for Ancient Field Morphology [J]. Geochemistry, Geophysics, Geosystems, 2021, e2021GC009930.*

<https://doi.org/10.1029/2021GC009930>

摘要：研究地磁场长期变化（PSV）可以对地磁场的平均的形态及地磁场发电机的运行过程提供参考。虽然近年来的研究提高了我们对中生代晚期古磁场行为的认识，但对三叠纪（约 251.9-201.3 Ma）的认识相对较少。本研究汇总了用于分析 PSV 的第一个三叠纪虚地磁极（VGP）数据库，也是更长的后-石炭-二叠反极性超时（PCRS）的一部分（265-198 Ma）。对比新的 PCRS 数据集及已出版的~320Ma 以来 PSV 结果，比较了 VGP 角度分布与视古纬度的依赖性。发现 VGP 散布在后-PCRS 几乎没有纬向变化，然而 PCRS 期间与纬度强相关。后-PCRS 的 PSV 行为展现出与之前报道的前-白垩纪正极性超时（Pre-CNS; 126-198 Ma）没有明显区别。这两个时间段内 PSV 行为一致，但是具有明显不同的视平均倒转频率，不支持 VGP 散布与倒转频率具有关系的假设。PCRS 期间 VGP 的散布与之前的研究一致，代表了在过去的 320 Ma 内可能具有独特的 VGP 行为。最近发表的方法从近赤道的 VGP 散布去获得地磁场形态的描绘展现出 PCRS 期间地磁场的轴向偶极子特征比其他任何时间间隔都要强。这个观测结果可能与 PCRS 是显生宙地磁极性年表内已知最长的超时相关。

ABSTRACT: Studying paleosecular variation (PSV) can provide unique insights into the average morphology of the geomagnetic field and the operation of the geodynamo. Although recent studies have expanded our knowledge of paleomagnetic field behavior through the late Mesozoic, relatively little is known regarding the Triassic period (ca. 251.9–201.3 Ma). This study compiles the first Triassic virtual geomagnetic pole (VGP) database for the analysis of PSV, as part of a longer Post-Permo-Carboniferous Reversed Superchron (PCRS) time interval (265-198 Ma). VGP angular dispersion and its dependence on apparent paleolatitude are compared against a new

PCRS compilation and published PSV compilations for intervals across the last ~320 Ma. We find that the Post-PCRS displays near latitudinal invariance of VGP dispersion while the PCRS displays very strong latitudinal dependence. PSV behavior during the Post-PCRS appears indistinguishable to that previously reported for the interval preceding the Cretaceous Normal Superchron (Pre-CNS; 126–198 Ma). The near-constant behavior between time intervals with significantly different apparent average polarity reversal frequencies does not support a suggested relationship between VGP dispersion and reversal frequency. The dispersion observed for the PCRS is consistent with the results of previous studies and represents behavior that is potentially unique over the last ~320 Ma. A recently published approach to obtain a description of field morphology from equatorial VGP dispersion shows the PCRS geomagnetic field to have been more strongly axial dipole dominated than any interval since. This observation may be causally linked to the PCRS being the longest known superchron in the Phanerozoic geomagnetic polarity timescale.

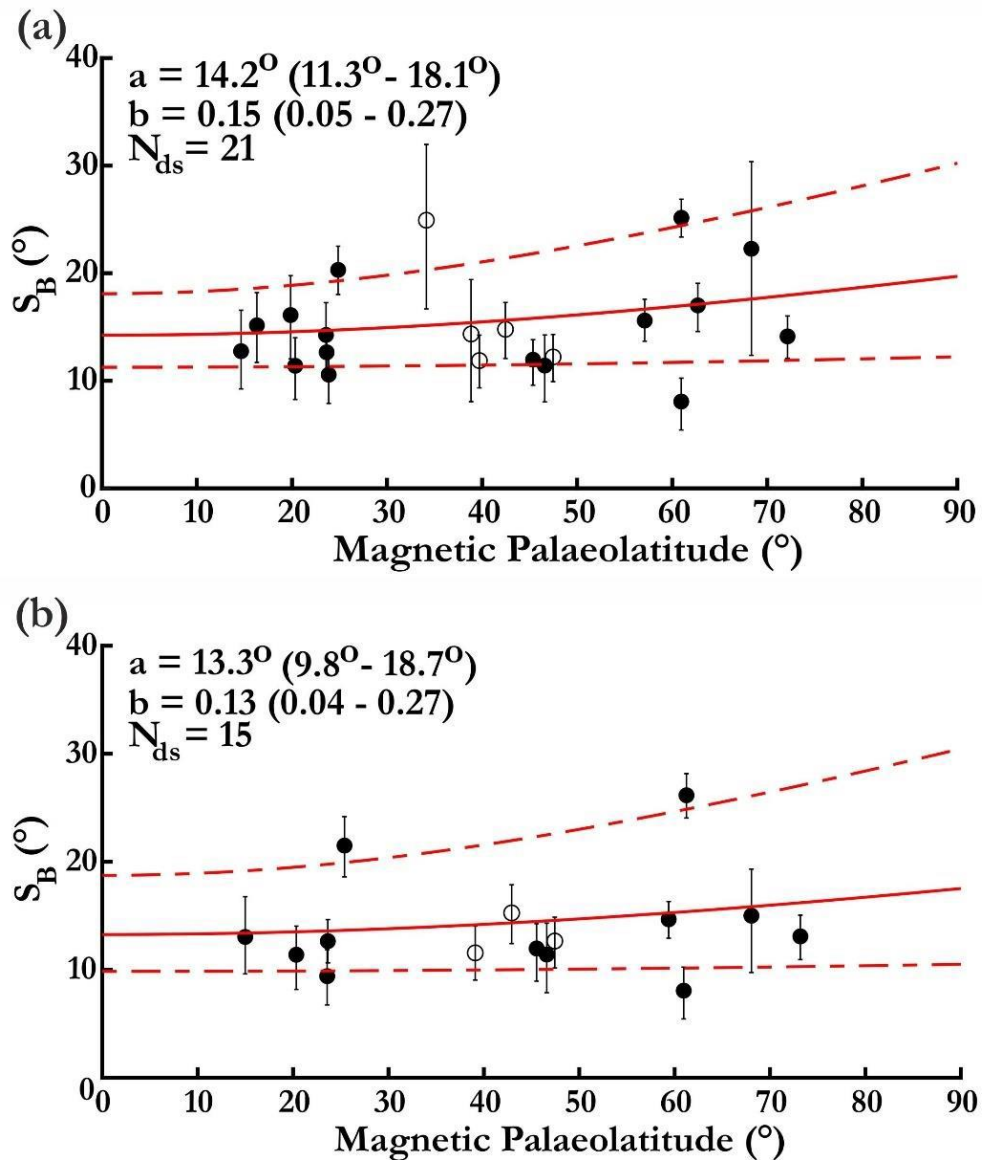


Figure 1. One hemisphere projection showing latitude dependence of virtual geomagnetic pole dispersion in the Post-PCRS (200-264 Ma). S_B values for northern and southern palaeolatitudes given by filled and empty circles respectively; error bars show their 95% confidence intervals. The solid red curve displays the best fit of Model G to the S_B values, dashed line represents the 95% confidence intervals given by the jack-knife method for 5000 replications. Estimates of Model G a and b shape parameters are displayed alongside their associated uncertainties and the number of datasets analysed (N_{ds}). a) displays datasets after application of Group 1 selection criteria, b) likewise for Group 2 criteria.

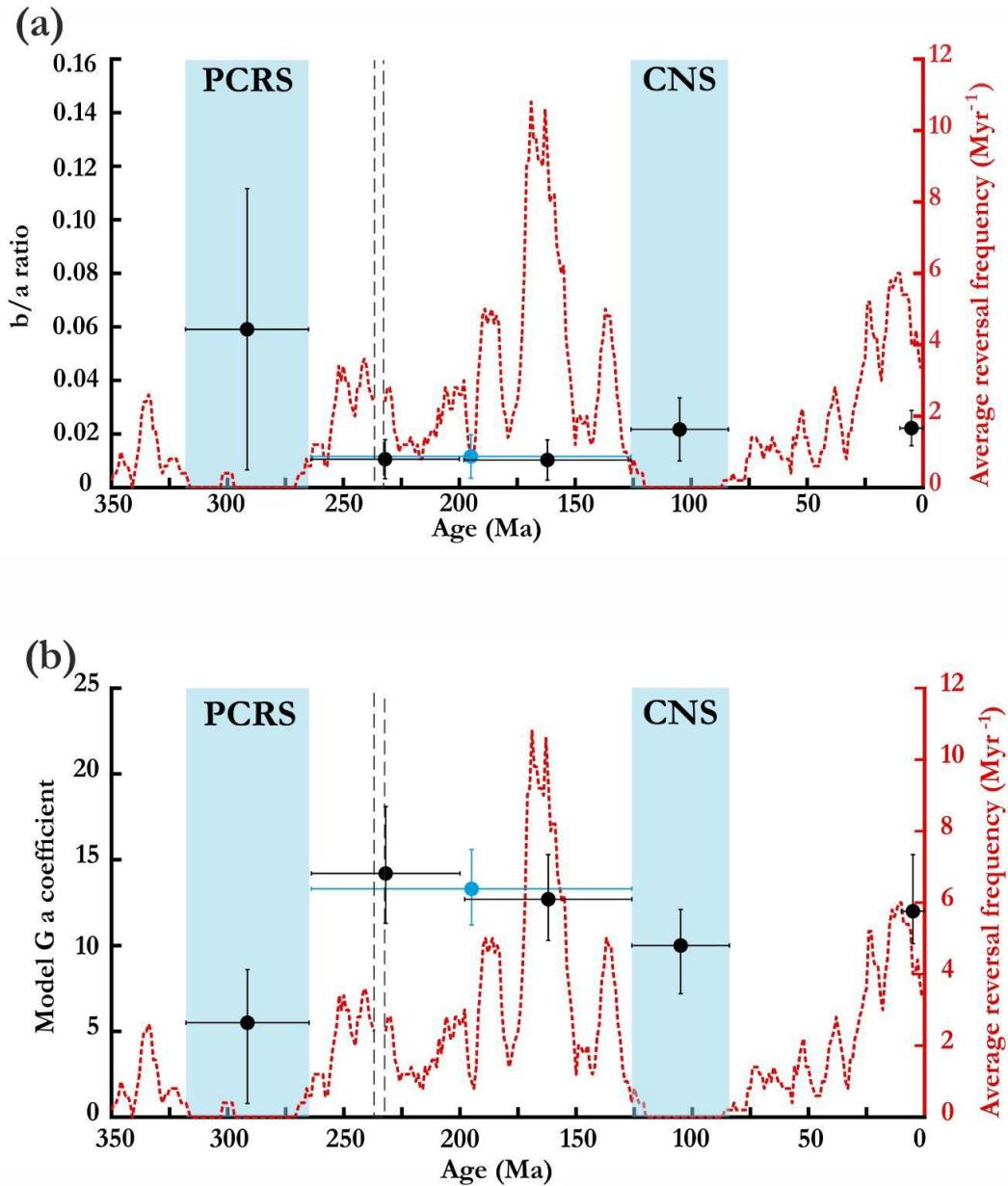


Figure 2. Variations in a) Model G b/a ratio b) Model G a parameter estimated for a range of time intervals. Last 10 Ma (0-10 Ma), (CNS (84-126 Ma), Pre-CNS (126-198 Ma), Post-PCRS (200-246 Ma), Pre-CNS & Post-PCRS (126-264 Ma), PCRS (265-318 Ma)). CNS & Pre-CNS data taken from Doubrovine et al. (2019), last 10 Ma data taken from Cromwell et al. 2018. Estimates of a) b/a ratio and b) Model g a parameter given by solid circles, vertical error bars represent the 95% confidence interval, horizontal error bars represent age range. The results displayed in blue are those from the combined database for the Post-PCRS and Pre-CNS. Dashed red line displays reversal frequency model constructed using a 5 Ma sliding window and magnetostratigraphic data from Ogg (2012) & Maron et al. (2019).

12. IODP U1504 孔多期碳酸盐岩脉记录了南海边缘早白垩世至早新生代伸展事件



翻译人：刘伟 inewway@163.com

Sun L, Sun Z, Zhang Y, et al. Multi-stage carbonate veins at IODP Site U1504 document Early Cretaceous to early Cenozoic extensional events on the South China Sea margin [J]. Marine Geology, 2021, 442: 106656.

<https://doi.org/10.1016/j.margeo.2021.106656>

摘要：厘定南海大陆边缘在南海打开之前的构造特征是理解南海如何打开的关键。然而，由于对变形事件缺乏直接的年代学约束，关于这一主题的研究极为匮乏。IODP U1504 孔在南海外缘高地基底获取了绿片岩相糜棱岩，这可以提供关于南海扩张前地质历史的信息。显微组份分析表明，糜棱岩受两次伸展作用的影响，即早期韧性变形和晚期脆性变形。根据与糜棱面理相交关系，确定了前糜棱期、同糜棱期和后糜棱期碳酸盐脉。前糜棱期碳酸盐脉的 U-Pb 年龄分别为 210 ± 20 Ma 和 195 ± 32 Ma，可能代表原岩的年龄。同糜棱期碳酸盐岩脉的年龄为 135 ± 12 Ma。对后糜棱期碳酸盐脉进行 U-Pb 测年，未获得有效年龄。后糜棱期碳酸盐岩脉的 $\delta^{13}\text{C}$ 、 $\delta^{18}\text{O}$ 和 $^{87}\text{Sr}/^{86}\text{Sr}$ 特征表明其形成于海水中的热液沉积作用环境。考虑到晚始新世以后北部大陆边缘广泛发育的海洋环境，U1504 孔的后糜棱期碳酸盐岩脉可能形成于始新世或更晚。根据显微构造、地球化学和地震剖面信息，推测后糜棱期碳酸盐岩脉形成于早新生代裂谷期。结合地质背景，我们认为南海边缘基底在扩张前至少经历了两个阶段的伸展：第一个阶段发生在早白垩世，是古太平洋板块的回转造成的；第二次发生在新生代早期，为被动裂谷作用。这些活动大陆边缘和被动大陆边缘的多次伸展事件共同导致南海大陆边缘变薄。

ABSTRACT: Recognition of the pre-spreading tectonic characteristics of the South China Sea (SCS) continental margin is key to understanding how the SCS opened. However, information on this subject is extremely scarce because of the lack of direct chronological constraints on deformation events. The International Ocean Discovery Program sampled greenschist-facies

mylonite from the basement of the Outer Margin High at site U1504 in the SCS, which could provide information on the pre-spreading history. The microstructure analysis revealed that two episodes of extension had affected the mylonites, namely early ductile and late brittle deformation. Pre-mylonite, syn-mylonite and post-mylonite carbonate veins were identified on the basis of the intersecting relationships with the mylonite foliation. The pre-mylonite carbonate veins yielded U–Pb ages of 210 ± 20 and 195 ± 32 Ma, which might represent the age of the protolith. The age of the syn-mylonite carbonate vein is 135 ± 12 Ma. No effective ages were obtained for the post-mylonite carbonate veins using U–Pb dating. The $\delta^{13}\text{C}$, $\delta^{18}\text{O}$ and $^{87}\text{Sr}/^{86}\text{Sr}$ compositions of the post-mylonite carbonate veins suggest that they were formed by hydrothermal fluid precipitation dominated by seawater. Considering the extensively developed marine environment in the northern continental margin after the late Eocene, the post-mylonite carbonate veins at site U1504 likely formed in the Eocene or later. Combining the microstructure, geochemistry and seismic profile, we hypothesize that post-mylonite carbonate veins were formed during early Cenozoic rifting. In reference to the geological background, we conclude that the basement of the SCS margin experienced at least two stages of extension before spreading: the first stage occurred during the Early Cretaceous and was caused by rollback of the Paleo-Pacific plate; the second occurred in the early Cenozoic because of passive rifting. These multiple extensional events of the active continental margin and of the passive margin collectively resulted in thinning the SCS continental margin.

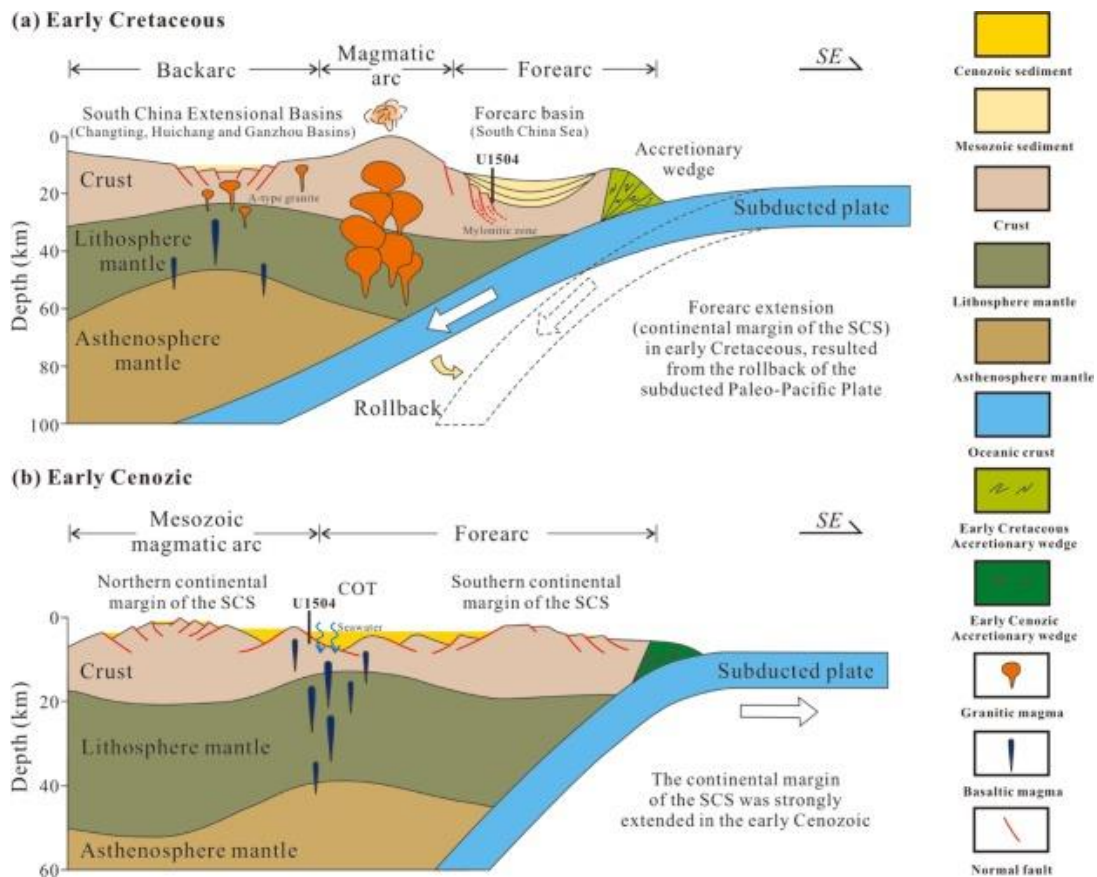


Figure 1. Conceptual model for the evolution of marginal basement in the SCS from early Cretaceous to early Cenozoic. (a) Due to the rollback of the subducted Pacific slab, the ductile deformation of the greenschist facies mylonite is caused by the extension in the forearc. (b) In the early Cenozoic, the continental margin of the SCS transitioned from active to passive continental margin as the proto-SCS subducting slab reversed its subduction direction (southward subduction). During passive extension, the continental margin of the SCS experienced intense stretching, thinning and magmatic upwelling, resulting in the late brittle deformation crosscutting the greenschist facies mylonite, such as fractures, crenulation cleavages, and carbonate veins. In general, the early ductile deformation of the greenschist facies mylonites records the early Cretaceous extensional movement in the continental margin of the SCS and the late brittle deformation records the early Cenozoic faulting. Abbreviations of tectonic units in the study area: COT – Continent-Ocean transition zone; SCS – South China Sea.